Potassium ion as kinetic controller in ionic double layer for hysteresis-free perovskite solar cell

Seul-Gi Kim[†a], Cheng Li[†b], Antonio Guerrero[†c], June-Mo Yang[a], Yu Zhong[b], Juan Bisquert[c]*, Sven Huettner[b]* and Nam-Gyu Park[a]*

[a]School of Chemical Engineering, Sungkyunkwan University (SKKU), Suwon 16419, Korea
[b]Department of Chemistry, University of Bayreuth, Universitätsstrasse 30, 95440 Bayreuth, Germany
[c]Institute of Advanced Materials (INAM) Universitat Jaume I, 12006 Castelló, Spain

[†]These authors equally contributed to this work
*Corresponding authors
J.B.: bisquert@uji.es
S.H.: sven.huettner@uni-bayreuth.de
N.-G. P.: npark@skku.edu, Tel: +82-31-290-7241

Publication:

Journal of Materials Chemistry A, 2019, 7, 18807–18815. Kim, S.G.; Li, C.; Guerrero, A.; Yang, J.M.; Zhong, Y.; Bisquert, J.; Huettner, S.; Park, N.G.

https://doi.org/10.1039/C9TA07595J

ABSTRACT

Since ion migration and interaction with the external contacts has been regarded as one of origins for photocurrent density (J)-voltage (V) hysteresis and phase segregation in perovskite solar cells (PSCs) under operational condition, control of ionic movement in organic-inorganic halide perovskite presents a big challenge for achieving hysteresis-free and stable PSCs. As a universal method, potassium doping proposed to bulk perovskite film to minimize or eliminate the hysteresis[1]. Here, we report direct observation of moderately retarded ion migration in K^+-doped $(FAPbI_3)_{0.875}(CsPbBr_3)_{0.125}$ perovskite by *in-situ* photoluminescence (PL) imaging. However, more impressive is the effect on the kinetics for generation of the ionic double layer at the vicinity of the contacts as it is reduced by two orders of magnitude in the time scale when devices are doped with K^+ as detected by impedance spectroscopy. A significantly reduced hysteresis in K^+-doped perovskite is responsible for more prolonged stability exhibiting ~96% of initial power conversion efficiency (PCE) after 22 days than relatively short-lived perovskite undoped with K^+ ion. This work highlights the clear correlation of ion migration and a fast generation of the double layer close to the contacts with severe hysteresis and long-term instability in PSCs and the importance of K^+ ion in reducing the kinetics affecting the ionic attachment to the contact surface.

Keywords: perovskite solar cell; hysteresis; ion migration; photo stability; doping; potassium

INTRODUCTION

Since the advent of a solid-state perovskite solar cell (PSC) with a power conversion efficiency (PCE) of 9.7% and 500 h-long-term-stability in 2012 [2], following two seed reports on perovskite-sanitized solar cells in 2009 and 2011 [3,4], perovskite photovoltaics have been burgeoned. As a result, a PCE as high as 23.7% was authorized by Newport Corp. as a proxy for National Renewable Energy Laboratory [5]. Although superb efficiency has

been achieved from PSCs, an issue, however, such as mismatch of current density (J)-voltage (V) curves depending on scan directions, termed J-V hysteresis, has been critically debated since 2014 [6] because the hysteresis could accelerate instability of PSCs [7]. The underlying factors affecting the J-V hysteresis include ferroelectric behavior associated with dipole orientation [8-10], native defects of perovskite [11-13], and accumulation of charged species at interfaces due to ion migration [14-18]. Methodologies to suppress the hysteresis have been proposed via enhancing charge transfer process at interfacial contacts [19-21], reduction or passivation of defects [19, 22-25] or preventing ions from migration by grain boundary passivation [26-30]. Heretofore, intrinsic defects of perovskite materials and interfaces have been suggested to play more critical role in the hysteresis for the highly efficient PSCs with substantially reduced hysteresis reported recently. Nevertheless, complete removal of the hysteresis is hard to be accomplished under continuous solar cell operating condition because slow ion conduction is intrinsic characteristics of organic-inorganic lead halide perovskite [31-33]. Recently, instead of indirect approaches such as interface passivation or compositional engineering, direct control of the ionic movement is considered to be more important because phase segregation and/or degradation in cation and/or anion mixed perovskite might be expected under operational condition [7, 34-38]. Therefore, a promising way to control the ionic movement effectively in bulk perovskite layer is essential for developing commercially available high-efficiency and long-term-stable PSCs. It was reported that a small amount of rubidium cation in the Cs/MA/FA mixed perovskite could improve PCE and photostability of PSCs [39]. In addition, a small amount of potassium ion was found to improve PCE in $MAPbI_3$ based PSCs [40]. Micro-mole scale potassium ion with respect to one mole of perovskite was first reported to have universal effect on reducing or eliminating the J-V hysteresis regardless of perovskite composition, which was explained

by prevention of Frenkel defects in bulk perovskite due to potassium ions stabilized in interstitial octahedral vacancies [1]. Stranks and coworkers have shown that potassium inhibits transient photoinduced ion-migration processes and prevents halide segregation both eventually reducing hysteresis in solar cells and improving stability [41]. Alternatively, Segawa and coworkers showed that a slight change in band positions, as measured by photoelectron spectroscopy, minimizes charge accumulation at the TiO_2 interface [42].

The ionic double layer is the structure that appears on the surface of a material when exposed to a liquid-like material. We have reported previously that under the presence of an electrical field hybrid perovskite materials behave like a liquid leading to ionic migration (i.e. ref 66 and Almora et al. Appl. Phys. Lett. 2016, 108, 043903). These ions accumulate at the external contact and form a double layer like in classic liquid electrochemistry. Observation of less- or non-hysteric behavior complemented by the use of different physical techniques. However, the precise formation kinetics of the double layer has not been reported in the presence of K^+ in operating devices that explains why potassium ion suppressed the hysteresis and ion migration. In this study, we show direct evidence that non-hysteric behavior is attributed to the kinetic stabilization of the ionic double layer in the perovskite at the interface with the external contacts. Perovskite/external contacts are studied by advanced impedance spectroscopy (IS) and electroabsorption (EA) spectroscopy. Alternatively, the ion migration in bulk perovskite is studied by *in-situ* photoluminescence (PL) imaging and calculation of the ion mobility shows that the effect of the K^+ doping only moderately decrease the ion mobility. Correlation between the stabilization of the ionic double layer and reduced supply of ions at the interfaces enables the achievement of hysteresis-free devices with increased stability.

RESULTS AND DISCUSSION

To investigate the effect of potassium ion dopant in $(FAPbI_3)_{0.875}(CsPbBr_3)_{0.125}$, mesoscopic normal PSCs were prepared including mesoporous TiO_2 (m-TiO_2) and spiro-MeOTAD (2,2',7,7'-tetrakis-(N,N-di-4-methoxyphenylamino)-9,9'-spirobifluorene) as shown in inset of **Fig. 1A**. Forward and reverse scanned J-V curves are measured depending on scan rate to understand the scan rate dependent hysteresis. **Fig. 1A and 1B** show J-V curves for the undoped and K^+-doped $(FAPbI_3)_{0.875}(CsPbBr_3)_{0.125}$ measured at scan rate of 13 mV/s, where forward-reverse scan is repeated with 5 cycles. Faster scan rates of 130 mV/s and 13,000 mV/s are also performed (**Fig. S1).** Photovoltaic properties depending on scan rate are listed in **Table S1**, where device structure is FTO/bl-TiO_2/mp-TiO_2/perovskite/spiro-MeOTAD/Au (bl in bl-TiO_2 stands for blocking layer). Control devices without K^+ doping show severe hysteric behavior and J-V hysteric structure depends on scan rate, whereas almost no hysteric property is observed upon K^+ doping regardless of scan rate. At very fast scan rate of 13000 mV/s, the control device shows small hysteresis that is unchanged on number of cycles (**Fig. S1A)**. When scan rate is reduced to 130 mV/s, hysteresis is pronounced but still invariable with cycles (**Fig. S1B)**. As compared to scan rate of 130 – 13000 mV/s, a large hysteresis is observed along with its strong dependence on repeating cycle at lower scan rate of 13 mV/s as shown in **Fig. 1A**. It is noted that the starting point (bias voltage showing difference in current between reverse and forward scan) from which hysteresis emerges is gradually decreased as the scan rate is decreased from 13000 mV/s to 130 mV/s and to 13 mV/s. These series of changes in hysteresis phenomenon with different scan rate and a huge change in J-V curves at slow scan rate are expected to be caused by the ion movement as discussed later. Thus, negligible hysteresis for the K^+-doped perovskite regardless of scan rate and scanning

cycles (**Fig. 1B**, **Fig. S1C** and **S1D**). In order to rule out possible contributions of the Li^+ additive used in spiro-MeOTAD and external contact layer which can role like pathway of ions, as Li^+ ion has been reported to migrate through the bulk of the perovskite layer [43, 44] and I^- ion migrate through spiro- MeOTAD layer [45], more simple configurations (FTO/perovskite/Au) confirm the hysteresis suppression as shown in **Fig. S2**. The movement of ion species can lead to formation of dipoles at the external interfaces and thereby modification in built-in potential [14, 30], which might correlate with hysteresis. This dynamic nature can be further probed by EA spectroscopy as it is known to be a noninvasive method to determine the built-in potential in solar cells as those induced by interfacial dipoles [16, 46, 47]. **Fig. S3** shows the change in the DC voltage dependent EA signal (ΔR/R) of PSCs employing perovskite without and with K^+ doping measured at photon energy of 1.63 eV under reverse and forward directions, respectively. Briefly, EA signal (ΔR/R), *i.e.* the change in the intensity of the reflected probe light in response to the external electric field modulation, vanishes when the external DC voltage compensates the built-in potential [48-50]. The characterized built-in potential reflects the influence of the accumulated ions at the opposite interfaces*, i.e.* perovskite/ETL or HTL [16]. For the control device, a built-in potential is established at $V_{forward}$=1.00±0.05 V for forward direction and at $V_{reverse}$=1.15±0.05 V for reverse direction. It is clear that the hysteresis behavior is observed during the EA measurement. However, for the device with K^+-doped perovskite, built-in potential is estimated to be almost identical regardless of scan direction ($V_{forward}$=1.15±0.05 V and $V_{reverse}$=1.10±0.05 V), which indicates that the internal electric field is invariant with scan direction due to less charge accumulation. To check the stability under continuous operating condition, the steady-state current density and PCE were measured for 100,000 s at the maximum power point under one sun illumination at 290 K in dry air (relative humidity (RH)

= 1.1%) as shown in **Fig. 1C** and **1D**. The steady-state PCE for the control device decreases from 16.66% at *t* = 200 s to 8.13% at *t* = 100,000 s (51.2% decrement), while the perovskite doped with K^+ ion is much more stable because of only 13% decrement after 100,000 s from 19.05% at *t* = 200 s to 16.55% at *t* = 100,000 s. Stability under one sun illumination was tested with devices, where devices were stored in dry air (RH = 1.1 %) under LED white light for certain intervals between measurements (24 h-interval from 0 h to 96 h and 48 h-interval from 96 h to 524 h). As shown in the **Fig. 1E**, the K^+ doped perovskite maintains its PCE up to 95.9% (reverse scan) and 94.3% (forward scan) of it is initial value after 528 h, while PCE of control device is significantly reduced to 75.6% (RS) and 62.7% (FS). The hysteresis index (HI) is calculated by eq 1 [25] and compared in **Fig. 1F.**

$$HI = \frac{\int_{SC}^{OC}(J_{RS}(V) - J_{FS}(V))dV}{\int_{SC}^{OC} J_{RS}(V)dV} \qquad (1)$$

The HI for the pristine perovskite is gradually increased from 0.20 to 0.36 after 528 h, indicating that hysteresis becomes severe. However, the K^+ doped perovskite shows little change in HI with time from 0.01 to 0.03. These results highlight the correlation between hysteresis and long-term stability.

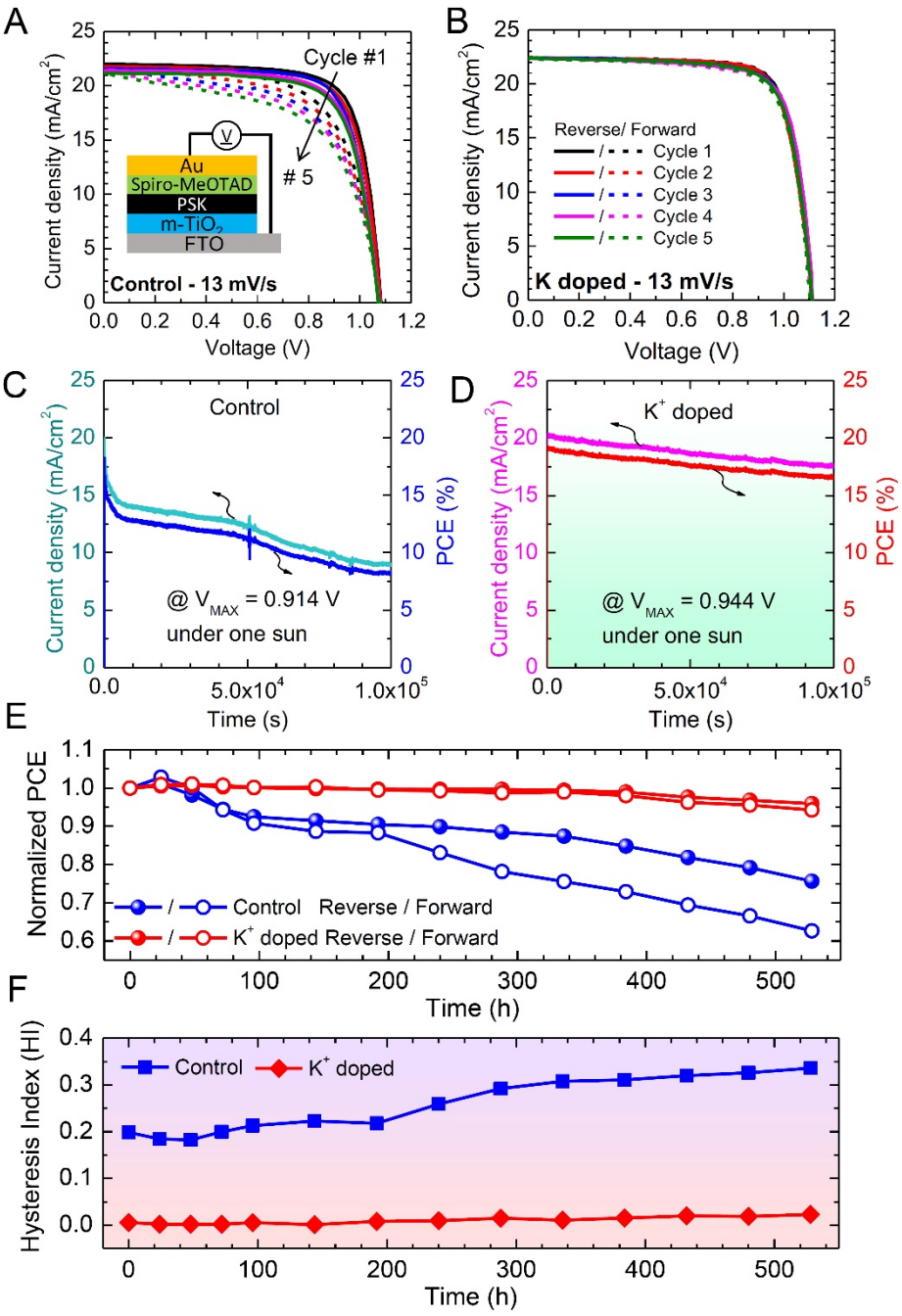

Fig. 1. J-V curves of perovskite solar cells employing $(FAPbI_3)_{0.875}(CsPbBr_3)_{0.125}$ perovskite (PSK) (A) without and (B) with K^+ ion ($[K^+]/[Pb^{2+}] = 0.01$). Inset in (A) shows the device structure for J-V measurement, where blocking TiO_2 layer was present between m-TiO_2 and FTO. Forward and reverse scanned J-V measurements were repeated 5 times at scan rate of 13 mV/s under AM 1.5G one sun illumination (100 mW/cm^2) at 293 K. Aperture mask area was 0.125 cm^2. Steady-state PCE and current density measured at voltage at maximum power point (V_{MAX}) under one sun illumination at 290 K in dry air condition (RH was 1.1%) for PCSs employing $(FAPbI_3)_{0.875}(CsPbBr_3)_{0.125}$ (C) without (control device) and (D) with K^+ doping. (E) Normalized PCE as a function of time measured at scan rate of 13 mV/s under

AM 1.5G one sun illumination (100 mW/cm2) at 290 K. The devices were kept under dry air and LED white light (97 mW/cm^2) condition. (F) Hysteresis index (HI) calculated based on the forward and reverse scanned data in (E).

In order to separate effects related to the bulk of the perovskite from interfacial phenomena we next measure the ion mobility in the bulk of the perovskite layer by *in-situ* photoluminescence (PL) imaging in a lateral configuration using a glass/m-TiO_2/perovskite/Au interdigitated structure (**Fig. 2**) [51, 52]. In this configuration, PL quenching takes place after polarization of the perovskite with an external bias in the form of a dark front which is related to transport of halide vacancies (V_I^+) in the bulk of the perovskite layer that can annihilate non-radiative recombination centers present in the perovskite. To exclude the influence from substrate to crystallization of PSK film, The PSK layer was deposited on m-TiO_2 /glass substrate and Au interdigitated electrodes are deposited on the perovskite layer with a spacing of 200 μm and the top of the device is covered with poly(methyl methacrylate) (PMMA) layer to protect the perovskite layer from moisture and oxygen during measurements (see the lateral structure in **Fig. 2G**). PL images are observed under 440 nm light illumination with a light intensity of 23.3 mW/cm^2 and an applied bias voltage (**Fig. 2A-2F**). Considering that ion conductivity can be remarkably increased under even weak light intensity [53], low bias voltages are applied from 0 V to 0.5 V with 0.1 V interval and the applied voltage is maintained for 300 s to see mainly halide migration. A custom-built optical microscope is used to obtain PL images [51, 54-56]. In case of the control device employing pristine $(FAPbI_3)_{0.875}(CsPbBr_3)_{0.125}$ without K^+ ion doping (see **Fig. 2A-2C** and **supplementary video 1**), the bright PL region at 0 V is narrowed as a bias voltage is applied and gradual PL quenching occurred near the positive Au electrode. The migration and accumulation of halide ions (Br^- and I^-) can have a direct effect on the PL

properties [57, 58]. In this case, the more mobile vacancies move within the applied electric field leaving behind remaining halide ion interstitials (I_i^- and Br_i^-). Those are prone to form deep defect states and acting as non-radiative recombination canters [24, 59-62]. For completeness we mention two further processes that can readily induce PL quenching such auger-like non-radiative recombination through ion accumulation [63-65] or even degradation of the perovskite structure. Doping with K^+ ions in the perovskite (**Fig. 2D-F)** shows a quite different spatial PL response under this low applied bias, where the bright PL region remains almost unchanged despite increasing the bias voltage, except for a few dark dots. A dark front is also observed at higher voltages of 4 V indicating that qualitatively ion mobility is reduced after K^+ doping. It is noticed that the PL is hard to be quenched even near positive electrode after potassium ion doping. The dynamic PL quenching process can be best observed in a video clip (**supplementary video 2**). The difference in PL images before and after K^+ doping is clear evidence that presence of potassium ion does affect ion migration dynamics in bulk perovskite without morphological change in perovskite as confirmed by SEM images in **Fig. S4**. However, a quantitative analysis is required in order to understand ion mobilities in the different samples. By measuring the current during the recording of PL images the ion mobility can be calculated as function of K^+ ratio. Here we use the dynamic transport model based on the modification of electronic concentration by the displacement of halide vacancies in the perovskites using eq 2 and eq 3 as described previously [52].

$$\frac{1}{j^2} = \frac{1}{j_0^2} + \frac{2\gamma v_0}{d j_0^2} t \qquad (2)$$

$$v_0 = \frac{p_0}{p_1}\frac{\mu_C V}{d} \qquad (3)$$

Where *d* is the distance, γ is the relative quantity of halide ion vacancies of total carriers (γ =

(p_0/p_1)-1 = (j_0/j)-1), p_0 and p_1 are the initial hole density in bright region and in the dark region, respectively, and v_0 is the initial velocity of ion and μ_C is the mobility of halide ion vacancies. The mobility of halide ion vacancies can be estimated by using the initial velocity of ions (v_0) which is extracted from slope of curves in the plot of the current as $1/j^2$ against time (t) with applied voltage of 4 V using interdigitated lateral device channel width of 150 μm as shown inset of **Fig. 2G**. **Fig. 2G** and **2H** show two representative examples and further data can be consulted in **Fig. S5** and **S6**. The estimated mobility of halide ion vacancies is gradually reduced from 2.46×10^{-6} cm/Vs (control w/o doping) to 1.18×10^{-6} cm/Vs ($[K^+]/[Pb^{2+}]=0.01$) and then increased to 1.53×10^{-6} cm/Vs ($[K^+]/[Pb^{2+}]=0.015$) (see **Fig. 2I**). As can be observed the ionic mobility in the bulk of the perovskite layer only decreases a factor of 2 during the addition of the K^+ additive. Therefore, the modest change in ionic mobility in the bulk of the perovskite layer cannot explain by itself the dramatic reduction in hysteresis. For this reason, we next apply a range of techniques to study the interfaces of perovskites with external contacts.

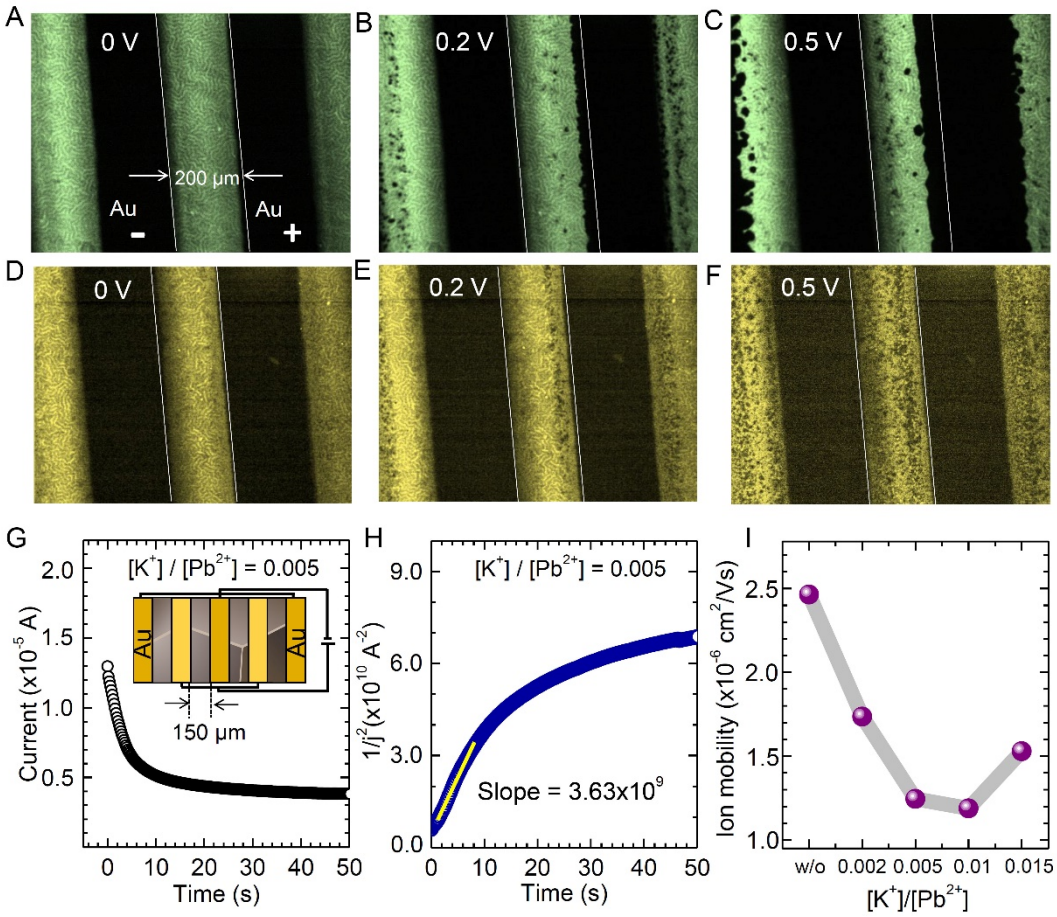

Fig. 2. Top-view *in-situ* photoluminescence (PL) images of bottom glass substrate/m-TiO_2/PSK/Au top electrodes (200 μm) devices employing (A-C) pristine $(FAPbI_3)_{0.875}(CsPbBr_3)_{0.125}$ perovskite (PSK) layer and (D-F) K^+-doped $(FAPbI_3)_{0.875}(CsPbBr_3)_{0.125}$ PSK layer obtained under 440 nm-light illumination with light intensity of 23.3 mW/cm^2 at different applied voltages from 0 V to 0.5 V with interval of 0.1 V (shown here is 0, 0.2 and 0.5 V. For the bias voltages PL images can be seen in video clips). PSK layers were covered with poly(methyl methacrylate) (PMMA) layer. Applied voltage was maintained for 300 s at a given bias voltage. Dark and bright images represent Au electrode and PSK layers, respectively. The "+" and "-" signs in (A) indicate polarity of the Au electrodes. the representative plot of (G) the current (j)-time(t) and (H) $1/j^2$ against time (t) with applied 4V voltage. (I) The estimated mobility of halide ion vacancies as a function of concentration of K^+ ion measured at interdigitated lateral devices with a channel width of 150 μm (inset of G) under 440 nm-light illumination with 23.3 mW/cm^2.

Alternatively, the effect on the external interfaces can be analyzed by using IS as it is possible to decouple bulk effects from external interfaces by the analysis of the capacitive and

resistive contributions to the measured current. For the purpose of this work, charge accumulation at the perovskite/Au interface can be monitored by analysis of the capacitance related to formation of an ionic double layer which is typically observed at low frequencies [66, 67]. In this technique, a DC voltage is applied to the sample and a small-signal AC voltage perturbation is superimposed with a wide range of frequencies. The frequency and amplitude of the AC perturbation modulates how much the system is separated from equilibrium and the extent to which carriers/ions will move in the oscillating field. The AC frequencies used for the experiments range from 1 MHz to 0.01 Hz. In this work, devices are designed to have Au/PSK/Au configuration with a channel width of 200 μm by using interdigitated electrodes as for PL experiments. As a reference device, we measure devices based on the simplest perovskite $MAPbI_3$ to understand ionic transport in this interdigitated configuration, which is compared with more complex systems having FA, Cs/ I, Br mixed ions without and with K^+ doping. **Fig. 3A** shows the capacitance vs frequency spectra of the interdigitated configurational lateral device in the dark at an applied DC potential of 0.2 V. At high frequency the dielectric capacitance of the perovskite layer is observed as a plateau at about 10-100 kHz and the capacitance increases for frequency values below 10 kHz. This increase in capacitance at low frequency is attributed to ion transport and accumulation at the external interfaces for measurements carried out in the dark generating an ionic double layer [68-70]. The $MAPbI_3$ device with interdigitated electrode shows a plateau in the low frequency range of 0.01-0.02 Hz due to the capacitance of the double layer of accumulated ions at the interfaces. Compared with $MAPbI_3$, perovskite with the complex system such as $(FAPbI_3)_{0.875}(CsPbBr_3)_{0.125}$ contains smaller ions (Br^- or Cs^+) than I^- and MA^+ and larger ion (FA^+) than MA^+. Then, ionic migration of these ion species is expected to simultaneously take place with different kinetic rates and shows the impedance response which shows the

result of the entire migrating species and perturbation of the ionic double layer. Interestingly, the whole capacitance curve is shifted towards lower frequencies, about one order of magnitude lower, indicating that the kinetics of ionic transport and accumulation is slower for $(FAPbI_3)_{0.875}(CsPbBr_3)_{0.125}$ in comparison to $MAPbI_3$. Finally, the K^+ ion doped $(FAPbI_3)_{0.875}(CsPbBr_3)_{0.125}$ shows that the ionic transport is considerably inactivated with capacitance curves shifted two orders of magnitude lower than control samples and three orders of magnitude in comparison to $MAPbI_3$.

A different way to visualize the same data is by using the complex impedance plot (**Fig. 3B-3D**) where ionic diffusion can be detected by formation of a 45º line for diffusion (Warburg element), a vertical line for ion accumulation and an ankle between the two regions with the characteristic frequency of diffusion (ω_d). As can be observed from **Fig. 3B**, the device containing $MAPbI_3$ clearly shows the transmission line that arises from ionic transport and an ankle at a frequency of 5.9 Hz which is the characteristic frequency at which ions the ionic double layer begins to be perturbed by accumulation at the external contacts. Fitting results to a model containing a transmission line show excellent fittings with errors below 10%. A complete analysis and comparison with systems containing RC elements are shown as **Fig. S7**, **S8** and **Table S2**. Similarly, the control device with $(FAPbI_3)_{0.875}(CsPbBr_3)_{0.125}$ in **Fig. 3C** shows the 45º line up to frequencies of 0.17 Hz when ions start to be accumulated and this frequency is one order of magnitude lower than that of $MAPbI_3$ in agreement with **Fig. 3B**. Alternatively, K^+ ion doped $(FAPbI_3)_{0.875}(CsPbBr_3)_{0.125}$ in **Fig. 3D** only shows the sign of ionic transport and the ankle is not observed even at frequencies as low as 10 mHz (the lowest frequency limit for this measurement), which can be interpreted that ionic transport is impeded by the presence of K^+ ion. Very importantly, the high frequency arc in the complex

impedance plot increases nearly two orders of magnitude when comparing the resistance from $MAPbI_3$ (0.09 MΩ), $(FAPbI_3)_{0.875}(CsPbBr_3)_{0.125}$ (0.6 MΩ), K^+-doped $(FAPbI_3)_{0.875}(CsPbBr_3)_{0.125}$ (6.5 MΩ). This high frequency arc obtained for measurements in the dark has been previously reported to be connected with charge transfer resistances through the external contacts [69]. In addition, as mobilities of vacancies, related to the bulk properties of the perovskites, are similar for $(FAPbI_3)_{0.875}(CsPbBr_3)_{0.125}$ and K^+-doped $(FAPbI_3)_{0.875}(CsPbBr_3)_{0.125}$ as measured by PL, then, it is clear that the increase in resistance is related to the properties of the contacts which are controlling the ion accumulation at the contacts. Here, we propose that under the presence of K^+ the kinetics to construct the surface polarization under illumination, related to hysteresis during measurements of J-V curves, is modified and we need a larger amount of iodine ions to build up the charge, as negatively charged iodine will be charge compensated by the K^+. In other words, the double layer capacitance is kinetically stabilized by K^+ and can only be perturbed at extremely low frequencies, with extrapolated values frequencies to obtain similar capacitances to that in the plateau in capacitance of frequencies < 0.001 Hz (>1000 s). Very importantly, at extremely slow scan rates (i.e. 0.1 mV/s) hysteresis is still observed for K^+-doped samples (see **Fig. S9**). For this reason, it is important to note that we have not totally removed the formation of the ionic double layer and, instead, its formation is slowed down by affecting the ionic attachment to the contact surface. We propose that this as a general physical process for previously reported “hysteresis-free” devices. These slow scan rates are not relevant for device operation conditions, however, they can be connected to degradation processes and understanding the kinetics of the double layer formation is a crucial point.

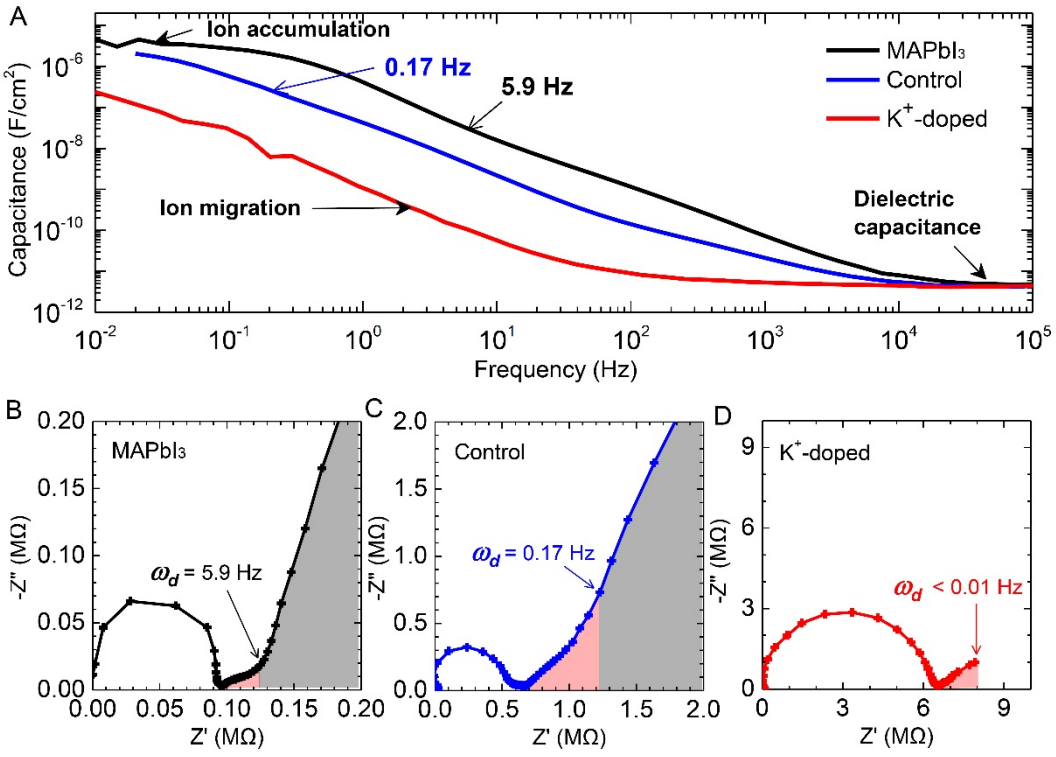

Fig. 3. (A) Capacitance-frequency plot and (B-D) complex impedance plot measured in the dark at 0.2 V for $MAPbI_3$, $(FAPbI_3)_{0.875}(CsPbBr_3)_{0.125}$ and K^+-doped $(FAPbI_3)_{0.875}(CsPbBr_3)_{0.125}$ perovskite. All measurements were conducted in the dark.

The precise mechanism of action of K^+ is currently under debate. The first central point of discussion is where exactly will be sitting the K^+ cations. These ions could be at the lattice interstices [1, 71] or segregated at the grain boundaries and close to the contacts by introducing a superlattice buffer layer at boundaries. [41, 72]. Lattice parameters must increase if K^+ ion in mixed composition is located in interstitial site in the lattice but should not change if K^+ is confined at the external interfaces. In addition, increase in lattice parameter is also probable by replacing Br^- anion in perovskite composition with iodide supplied by KI. To figure out the probable location of K^+ ion, we measure XRD of $(FAPbI_3)_{0.875}(CsPbI_3)_{0.125}$ before and after KBr doping in order to investigate change of lattice

parameter in the absence of lattice bromide using a freeware of EXPO2014 program as shown in **Fig. S10**[73], together with $(FAPbI_3)_{0.875}(CsPbBr_3)_{0.125}$ before and after KI addition. Both $(FAPbI_3)_{0.875}(CsPbBr_3)_{0.125}$ and $(FAPbI_3)_{0.875}(CsPbI_3)_{0.125}$ are indexed as cubic phase with space group of Pm^{-},3m. The XRD peaks are gradually shifted to lower angles by 0.07~0.1º upon doping KI and KBr in both $(FAPbI_3)_{0.875}(CsPbBr_3)_{0.125}$ and $(FAPbI_3)_{0.875}(CsPbI_3)_{0.125}$ (see **Fig. S10)**. The lattice parameter of $(FAPbI_3)_{0.875}(CsPbBr_3)_{0.125}$ increases gradually from 6.280305± 0.000669 Å to 6.298689 ± 0.000553 Å (**Fig. S10A** and **B**) and to 6.288922 ± 0.000475 (**Fig. S10C** and **D**) as $[K^+]/[Pb^{2+}]$ increases from 0 to 0.01 by doping with KI and KBr, respectively. For $(FAPbI_3)_{0.875}(CsPbI_3)_{0.125}$, the lattice parameter is enlarged from 6.321077±0.001389 Å to 6.333954 ± 0.000503 Å (**Fig. S10E** and **F**) and to 6.328712 ± 0.000551 (**Fig. S10G** and **H**) as $[K^+]/[Pb^{2+}]$ increases from 0 to 0.01 by doping with KI and KBr, respectively. Lattice expansion is concluded to be due to K ion rather than replacement of bromide with iodide because lattice expansion observed in KBr doped $(FAPbI_3)_{0.875}(CsPbI_3)_{0.125}$ is decisively indicative of interstitial location of K^+ ion. XPS depth profiling measurements give a very similar image, of equal K^+ content throughout the hole film with an apparent increase of K^+ content at the mesoporous electrode (**Fig. S11**). We measured PL and TRPL by using PSK film and bl-TiO_2/ ms-TiO_2/ PSK devices to find out the influence of K^+ ion to charge extraction at the interface between PSK and TiO_2 (**Fig. S12 and Table S2**). PL intensity of $(FAPbI_3)_{0.875}(CsPbBr_3)_{0.125}$ with K^+ ion is about 3 times enhanced. Also, the amplitude of τ_1 (A_1) increased from 72.8 % for w/o K to 19.3% for K doped. Suppression of nonradiative recombination is might indicative of the decrease in the trap density.[1] Steady state PL shows that PL quenching is observed at bl-TiO_2/m-TiO_2/$(FAPbI_3)_{0.875}(CsPbBr_3)_{0.125}$ interfaces. TRPL spectra of the $(FAPbI_3)_{0.875}(CsPbBr_3)_{0.125}$

perovskite film without and doped with K^+ ion in contact with m-TiO_2 shows amplitude of τ_1 (A_1) of K doped one is (87.3%) slightly higher than without K ion in PSK (84.9%). This means electron extraction at the interface of K^+ doped PSK/ m-TiO_2 is better than without one. Alternatively, if K^+ ion is phase segregated and generates a buffer superlattice close to the grain boundaries and external contacts capacitive contributions related to the kinetics of the generation of the double layer will be modified. Note that this chemical effect is not specific for monovalent cations as hysteresis has also been suppressed for Rb^+, other small mobile cations like Li^+ could lead to additional effects related to migration of the additives under an applied electrical field. In this respect, impedance spectroscopy clearly shows differences of two orders of magnitude, control $(FAPbI_3)_{0.875}(CsPbBr_3)_{0.125}$ samples compared with K^+-doped one, in the polarization time of the double layer. Here, we propose that remaining K^+ at the external contacts will strongly interact with migrating iodine ions by reducing the kinetics of formation of the double layer. i.e. Ti^{3+} defects present at TiO_2 will be less prone to interact with migrating I^-. Therefore, we can conclude that K^+ ions placed at the contacts will play a major role in the kinetics stabilization of the double layer which will ultimately determine the hysteresis behavior and degradation kinetics.

CONCLUSION

We showed a clear correlation between double layer polarization, hysteresis and long term degradation of devices. A gradual increase in hysteresis was observed for the pristine perovskite without K^+ doping as per long-term stability test, while almost no change in hysteresis was observed for the K^+-doped perovskite. The origin of the hysteresis was studied by decoupling bulk effects in the perovskite to those related to the external contacts.

Moderate retarded ion movement in the bulk of the perovskite is induced by K^+ doping as confirmed by *in-situ* PL measurements. Real time PL images proved directly directional ionic mobility in mixed perovskite $(FAPbI_3)_{0.875}(CsPbBr_3)_{0.125}$ at applied voltage from 0 V to 0.5 V, which is reduced by K^+ doping. A dynamic transport model based on the modification of electronic concentration by the displacement of halide vacancies in the perovskites allows the calculation of the ion mobilities. Interfacial effects induced by K^+ doping is probed by IS and it is shown that the kinetics of formation of the double layer is highly influenced by this cation. This work highlights that ion migration plays a critical role of K^+ doping in reducing hysteresis and long-term instability in PSCs by modification of the kinetics in the generation of the double layer at the vicinity of the contacts. We propose that the kinetics of ionic attachment to the contact surface determines the kinetics of hysteresis as a general physical process for previously reported "hysteresis-free" devices.

ACKNOWLEDGEMENTS

We are very grateful to H. Segawa for discussions. This work was supported by the National Research Foundation of Korea (NRF) grants funded by the Ministry of Science, ICT Future Planning (MSIP) of Korea under contracts NRF-2012M3A6A7054861 and NRF-2014M3A6A7060583 (Global Frontier R&D Program on Center for Multiscale Energy System) and NRF-2016M3D1A1027663 and NRF-2016M3D1A1027664 (Future Materials Discovery Program) and NRF-2018K2A9A2A15075785 / DAAD (Germany-Korea Partnership Program (GEnKO Program)). S.H., C.L. and Y.Z. thank the DFG (German research foundation) and the Bavarian framework program Soltech for financial support. Y.Z. thanks the CSC for their support. This work was also supported by Basic Science Research

Program through the NRF under contact 2016R1A2B3008845 and NRF-2017H1A2A1046990 (NRF-2017-Fostering Core Leaders of the Future Basic Science Program/Global Ph.D. Fellowship Program). A.G. and J.B. acknowledge funding from Ministerio de Economíay Competitividad of Spain (MAT2016-76892-C3-1-R and RYC-2014-16809).

REFERENCES

(1) D.-Y. Son, S.-G. Kim, J.-Y. Seo, S.-H. Lee, H. Shin, D. Lee, N.-G. Park, *J. Am. Chem. Soc*., 2018, **140**, 1358–1364.

(2) H.-S. Kim, C.-R. Lee, J.-H. Im, K.-B. Lee, T. Moehl, A. Marchioro, S.-J. Moon, R. Humphry-Baker, J.-H. Yum, J. E. Moser, M. Grätzel, N.-G. Park, *Sci. Rep*., 2012, **2**, 591.

(3) A. Kojima, K. Teshima, Y. Shirai, T. Miyasaka, *J. Am. Chem. Soc*., 2009, **131**, 6050−6051.

(4) J.-H. Im, C.-R. Lee, J.-W. Lee, S.-W. Park, N.-G. Park, *Nanoscale*., 2011, **3**, 4088−4093.

(5) https://www.nrel.gov/pv/assets/pdfs/pv-efficiency-chart.20190103.pdf

(6) H. J. Snaith, A. Abate, J. M. Ball, G. E. Eperon, T. Leijtens, N. K. Noel, S. D. Stranks, J. T. Wang, K. Wojciechowski, W. Zhang, *J. Phys. Chem. Lett*. 2014, **5**, 1511−1515.

(7) N.-G. Park, M. Grätzel, T. Miyasaka, K. Zhu, K. Emery, *Nat. Energy*., 2016, **1**, 16152.

(8) H.-W. Chen, N. Sakai, M. Ikegami, T. *J.* Miyasaka*, Phys. Chem. Lett*., 2015, **6**, 164−169.

(9) J. M. Frost, K. T. Butler, A. Walsh, *APL Mater*., 2014, **2**, 081506.

(10) A. M. A. Leguy, J. M. Frost, A. P. McMahon, V. G. Sakai, W. Kockelmann, C. Law, X. Li, F. Foglia, A. Walsh, B. C. O'Regan, J. Nelson, J. T. Cabral, P. R. F. Barnes, *Nat. Commun*., 2015, **6**, 7124.

(11) D. W. Miller, G. E. Eperon, E. T. Roe, C. W. Warren, H. J. Snaith, M. C. Lonergan,

Appl. Phys. Lett., 2016, **109**, 153902.

(12) H. Yu, H. Lu, F. Xie, S. Zhou, N. Zhao, *Adv. Funct. Mater*., 2016, **26**, 1411–1419.

(13) D. Yang, W. Ming, H. Shi, L. Zhang, M.-H. Du, *Chem. Mater*., 2016, **28**, 4349−4357.

(14) J. M. Azpiroz, E. Mosconi, J. Bisquert, F. D. Angelis, *Energy Environ. Sci*., 2015, **8**, 2118−2127.

(15) H.-S. Kim, I.-H. Jang, N. Ahn, M. Choi, A. Guerrero, J. Bisquert, N.-G. Park, *J. Phys. Chem. Lett*., 2015, **6**, 4633−4639.

(16) C. Li, S. Tscheuschner, F. Paulus, P. E. Hopkinson, J. Kießling, A. Köhler, Y. Vaynzof, S. Huettner, *Adv. Mater*., 2016, **28**, 2446−2454.

(17) G. Richardson, S. E. J. O'Kane, R. G. Niemann, T. A. Peltola, J. M. Foster, P. J. Cameronc, A. B. Walker, *Energy Environ. Sci*., 2016, **9**, 1476−1485.

(18) H. Wang, A. Guerrero, A. Bou, A. A. Mayouf, J. Bisquert, *Energy Environ. Sci***.**, 2019, Advance Article (2019). DOI :10.1039/C9EE00802K.

(19) S.-G. Kim, J. Chen, J.-Y. Seo, D.-H. Kang, N.-G. Park, *ACS Appl. Mater. Interfaces*., 2018, **10**, 25372−25383.

(20) H. -S, Yoo, N.-G. Park, *Sol. Energy Mater. Sol. Cells*., 2018, **179**, 57-65.

(21) G. Chen, F. Zhang, M. Liu, J. Song, J. Lian, P. Zeng, H.-L. Yip, W. Yang, B. Zhang, Y. Cao, *J. Mater. Chem. A.*, 2017, **5**, 17943–17953.

(22) X. Zheng, B. Chen, J. Dai, Y. Fang, Y. Bai, Y. Lin, H. Wei, X. C. Zeng, J. Huang, *Nat. Energy*., 2017, **2**, 17102.

(23) T. Zhao, C.-C. Chueh, Q. Chen, A. Rajagopal, A. K.-Y. Jen, *ACS. Energy. Lett*., 2016, **1**, 757–763.

(24) W. S. Yang, B.-W. Park, E. H. Jung, N. J. Jeon, Y. C. Kim, D. U. Lee, S. S. Shin, J. Seo, E. K. Kim, J. H. Noh, S. I. Seok, *Science*., 2017, **356**, 1376–1379.

(25) J.-W. Lee, S.-G. Kim, S.-H. Bae, D.-K. Lee, O. Lin, Y. Yang, N.-G. Park, *Nano Lett*., 2017, **17**, 4270–4276.

(26) H.-S. Kim, N.-G. Park, *J. Phys. Chem. Lett.*, 2014, **5**, 2927–2934.

(27) D.-Y. Son, J.-W. Lee, Y. J. Choi, I.-H. Jang, S. Lee, P. J. Yoo, H. Shin, N. Ahn, M. Choi, D. Kim, N.-G. Park, *Nat. Energy.,* 2016, **1**, 16081.

(28) J. Chen, D. Lee, N.-G. Park, *ACS Appl. Mater. Interfaces*. 2017, **9**, 36338-36349.

(29) Y. Lin, Y. Bai, Y. Fang, Q. Wang, Y. Deng, J. Huang, *ACS Energy Lett*., 2017, **2**, 1571−1572.

(30) J.-W. Lee, Z. Dai, T.-H. Han, C. Choi, S.-Y. Chang, S.-J. Lee, N. D. Marco, H. Zhao, P. Sun, Y. Huang, Y. Yang, *Nat. Commun*., 2018, **9**, 3021.

(31) C. Eames, J. M. Frost, P. R. F. Barnes, B. C. O'Regan, A. Walsh, M. S. Islam, *Nat. Commun.*, 2015, **6**, 7497.

(32) J. Xing, Q. Wang, Q. Dong, Y. Yuan, Y. Fanga, J. Huang, *Phys. Chem. Chem. Phys.*, 2016, **18**, 30484−30490 (2016)

(33) T. Wu, M. Ahmadi, B. Hu, *J. Mater. Chem. C.*, 2018, **6**, 8042−8050.

(34) Y. Yuan, J. Huang, *Acc. Chem. Res*., 2016, **49**, 286−293.

(35) E.T. Hoke, D. J. Slotcavage, E. R. Dohner, A. R. Bowring, H. I. Karunadasa, M. D. McGehee, *Chem. Sci*., 2015, **6**, 613–617.

(36) B. Rivkin*,* P. Fassl, Q. Sun, A. D. Taylor, Z. Chen, Y. Vaynzof, *ACS Omega*., 2018, **3**, 10042−10047.

(37) S. Kim, S. Bae, S.-W. Lee, K. Cho, K. D. Lee, H. Kim, S. Park, G. Kwon, S.-W Ahn, H.-M. Lee, Y. Kang, H.-S. Lee, D. Kim. *Sci. Rep*., 2017, **7**, 1200.

(38) S. Cacovich, L. Ciná, F. Matteocci, G. Divitini, P. A. Midgley, A. Di Carlob, C. Ducati, *Nanoscale.*, 2017, **9**, 4700–4706.

(39) M. Saliba, T. Matsui, K. Domanski, J.-Y. Seo, A. Ummadisingu, S. M. Zakeeruddin, J.-P. Correa-Baena, W. R. Tress, A. Abate, A. Hagfeldt, M. Grätzel, *Science*., 2016, **354**, 206–209.

(40) P. Zhao, W. Yin, M. Kim, M. Han, Y. J. Song, T. K. Ahn, H. S. Jung, *J. Mater. Chem. A.*, 2017, **5**, 7905–7911.

(41) M. Abdi-Jalebi, Z.Andaji-Garmaroudi, S. Cacovich, C. Stavrakas, B. Philippe, J. M. Richter, M. Alsari, E. P. Booker, E. M. Hutter, A. J. Pearson, S. Lilliu, T. J. Savenije, H. Rensmo, G. Divitini, C. Ducati, R. H. Friend, S. D. Stranks, *Nature,* 2018, **555**, 497–501.

(42) Z Tang, T. Bessho, F. Awai, T. Kinoshita, M. M. Maitani, R. Jono, T. N. Murakami, H. Wang, T. Kubo, S. Uchida, H. Segawa, *Sci. Rep.,* 2017, **7**, 12183.

(43) N. Vicente, G. Garcia-Belmonte, *Adv. Energy Mater*., 2017, **7**, 1700710.

(44). Z. Li, C. Xiao, Y. Yang, S. P. Harvey, D. H. Kim, J. A. Christians, M. Yang, P. Schulz, S. U. Nanayakkara, C.-S. Jiang, J. M. Luther, J. J. Berry, M. C. Beard, M. M. Al-Jassima, K. Zhu, *Energy Environ. Sci*., 2017, **10**, 1234-1242.

(45) C. Besleaga, L. E. Abramiuc, V. Stancu, A. G. Tomulescu, M. Sima, L. Trinca, N. Plugaru, L. Pintilie, G. A. Nemnes, M. Iliescu, H. G. Svavarsson, A. Manolescu, I. Pintilie, *J. Phys. Chem. Lett*., 2016, **7**, 5168-5175

(46) X. Wu, H. Yu, L. Li, F. Wang, H. Xu, N. Zhao, *J. Phys. Chem. C, 2015,* **119**, 1253–1259.

(47) V. Roiati, E. Mosconi, A. Listorti, S. Colella, G. Gigli, F. D. Angelis, *Nano Lett*., 2014, **14**, 2168–2174.

(48) C. Li, Y. Vaynzof, G. Lakhwani, G. J. Beirne, J. Wang, N. C. Greenham, *J Appl. Phys,* 2017, **121**, 144503.

(49) H. Tsai, R. Asadpour, J.-C. Blancon, C. C. Stoumpos, O. Durand, J. W. Strzalka, B. Chen, R. Verduzco, P. M. Ajayan, S. Tretiak, J. Even, M. A. Alam, M. G. Kanatzidis, W. Nie, A. D. Mohite, *Science*, 2018, **360**, 67–70.

(50) F.-J. Kahle, C. Saller, S. Olthof, C. Li, J. Lebert, S. Wei, E. M. Herzig, S. Huettner, K. Meerholz, P. Strohriegl, A. Köhler, *J. Phys. Chem. C*, 2018, **122**, 21792−21802.

(51) C. Li, A. Guerrero, Y. Zhong, A. Gräser, C. A. M. Luna, J. Köhler, J. Bisquert, R. Hildner, S. Huettner, *Small*., 2017, **13**, 1701711.

(52) C. Li, A. Guerrero, S. Huettner, J. Bisquert, *Nat. Commun*., 2018, **9**, 5113.

(53) G, Y. Kim, A. Senocrate, T.-Y. Yang, G. Gregori, M. Grätzel, J. Maier, *Nat. Mater*., 2018, **17**, 445-449.

(54) A. Issac, R. Hildner, C. Hippius, F. Würthner, J. Köhler. *ACS Nano.*, 2018, **8**, 2, 1708-1717.

(55) C. Li, Y. Zhong, C. A. M. Luna, T. Unger, K. Deichsel, A. Gräser, J. Köhler, A. Köhler, R. Hildner, Sven Huettner, *Molecules.*, 2016, **21**, 1081.

(56) A.T. Haedler, K. Kreger, A. Issac, B, Wittmann, M, Kivala, N. Hammer, J. Köhler, H.-W. Schmidt, R. Hildner, *Nature*., 2015, **523**, 196–199.

(57) S. Chen, X. Wen, R. Sheng, S. Huang, X. Deng, M. A. Green, A. Ho-Baillie, *ACS Appl. Mater. Interfaces*., 2016, **8**, 5351−5357.

(58) D. L. Jacobs, M. A. Scarpulla, C. Wang, B. R. Bunes, L. Zang, *J. Phys. Chem. C*., 2016, **120**, 7893-7902.

(59) A. Buin, P. Pietsch, J. Xu, O. Voznyy, A. H. Ip, R. Comin, E. H. Sargent, *Nano Lett.*, 2014, **14**, 6281-6286.

(60) D. Meggiolaro, S. G. Motti, E. Mosconi, A. J. Barker, J. Ball, C. A. R. Perini, F. Deschler, A. Petrozza, F. D. Angelis, *Energy Environ. Sci*., 2018, **11**, 702-713.

(61) W.-J. Yin, T. Shi, Y. Yan, *Appl. Phys. Lett.*, 2014, **104**, 063903.

(62) X. Deng, X. Wen, C. F. J. Lau, T. Young, J. Yun, M. A. Green, S. Huang, A. W. Y. Ho-Baillie, *J. Mater. Chem. C*, 2016, **4**, 9060-9068.

(63) X. Wen, A. Ho-Baillie, S. Huang, R. Sheng, S. Chen, H.-C. Ko, M. A. Green, *Nano Lett.,*

2015, **15**, 4644−4649.

(64) A.L. Efros, M. Rosen, *Phys. Rev. Lett.,* 1997, **78**, 1110-1113.

(65) C. Galland, Y. Ghosh, A. Steinbrück, M. Sykora, J. A. Hollingsworth, V. I. Klimov, H. Htoon, *Nature.,* 2011, **479**, 203−207.

(66) W. Peng, C. Aranda, O. M. Bakr, G. Garcia-Belmonte, J. Bisquert, A. Guerrero, *ACS Energy Lett.,* 2018, **3**, 1477-1481.

(67) J. Bisquert, *Phys. Chem. Chem. Phys.*, 2000, **2**, 4185-4192..

(68) J. Bisquert, A. Compte, *J. Electroanal. Chem*., 2001, **499**, 112-120.

(69) A. Guerrero, G. Garcia-Belmonte, I. Mora-Sero, J. Bisquert, Y. S. Kang, T. J. Jacobsson, J.-P. Correa-Baena, *J. Phys. Chem. C.,* 2016, **120**, 8023-8032.

(70) O. Almora, I. Zarazua, E. Mas-Marza, I. Mora-Sero, J. Bisquert, G. Garcia-Belmonte, *J. Phys. Chem. Lett*., 2015, **6**, 1645-1652.

(71) J. Cao, S. X. Tao, P. A. Bobbert, C.-P. Wong, N. Zhao*, Adv. Mater*., 2018, **30**, 1707350.

(72) T. W. Kim, S. Uchida, T. Matsushita, L. Cojocaru, R. Jono, K. Kimura, D. Matsubara, M. Shirai, K. Ito, H. Matsumoto, T. Kondo, H. Segawa, *Adv. Mater*., 2018, **30**, 1705230.

(73) A. Altomare, C. Cuocci, C. Giacovazzo, A. Moliterni, R. Rizzi, N. Corriero, A. Falcicchio, *J. Appl. Crystallogr*., 2013, **46**, 1231–1235.

Supporting Information

Potassium ion as kinetic controller in ionic double layer for hysteresis-free perovskite solar cell

Seul-Gi Kim[†a], Cheng Li[†b], Antonio Guerrero[†c], June-Mo Yang[a], Yu Zhong[b], Juan Bisquert[c]*, Sven Huettner[b]* and Nam-Gyu Park[a]*

[a]School of Chemical Engineering, Sungkyunkwan University (SKKU), Suwon 16419, Korea
[b]Department of Chemistry, University of Bayreuth, Universitätsstrasse 30, 95440 Bayreuth, Germany
[c]Institute of Advanced Materials (INAM) Universitat Jaume I, 12006 Castelló, Spain

Experimental section

Materials Synthesis

Formamidinium iodide (FAI) or methylammonium iodide (MAI) was synthesized by reacting 30 mL hydroiodic acid (57 wt% in water, Sigma-Aldrich) with 15 g of formamidinium acetate (99%, Aldrich) or 27.8 mL of methylamine (40 wt% in methanol, TCI) in ice bath. After stirring for 30 min, brown precipitate was formed by evaporating the solvent at 60 °C using rotary evaporator. The solid powder was washed with diethyl ether (99.0%, SAMCHUN) several times, which was followed by recrystallization in anhydrous ethanol. The white precipitate was filtered and dried under vacuum for 24 h, which was stored in a glove box filled with Ar.

Device Fabrication

The patterned FTO glass (Pilkington, TEC-8, 8Ω/sq) was ultrasonically cleaned with detergent and DI water. Ultraviolet-Ozone (UVO) was treated for 40 min to remove organic contaminants. The blocking TiO_2 (bl-TiO_2) layer was deposited on the cleaned FTO substrate by immersing substrate in 20 mM aqueous $TiCl_4$ (99.9%, Sigma-Aldrich) solution at 70 °C for 20 min, washing with DI water and annealing at 500 °C for 30 min. After cooling down to

room temperature, the film was exposed to UVO for 40 min before coating a mesoporous TiO_2 (m-TiO_2) layer. The m-TiO_2 layer was deposited by spin-coating a TiO_2 paste (particle size of ~50 nm, ShareChem) diluted in 1-butanol (0.1 g/mL) at 2000 rpm for 20 s, which was annealed at 550 ºC for 30 min. The annealed TiO_2 film was further treated with 20 mM aqueous $TiCl_4$ (Sigma-Aldrich, > 98%) solution at 70 ºC for 10 min and then annealed again at 500 ºC for 30 min. For deposition of $(FAPbI_3)_{0.875}(CsPbBr_3)_{0.125}$ perovskite, a precursor solution was prepared by mixing 0.1505 g of FAI, 0.4034 g of PbI_2 (99.99%, TCI), 0.0459 g of $PbBr_2$ (99.999%, Alfa Aesar) and 0.0266 g of CsBr (99.999%, Sigma Aldrich) in 0.53 mL of *N,N'*-dimethylformamide (DMF, 99.8% anhydrous, Sigma Aldrich) and 0.75 μL *N*,*N*-dimethylsulfoxide (DMSO, >99.5%, Sigma Aldrich). For K^+ doping, 10 mM of KI stock solution in DMF was prepared by dissolving 0.166 g of KI (≥ 99.99% trace metals basis, Sigma Aldrich) in 10 mL of DMF and 0.1 mL of DMF in perovskite precursor solution was replaced by the KI stock solution to make ratio of K^+ to Pb^{2+} 0.01 ([K]/[Pb]=0.01). The solutions were filtered with 0.20 μm pore sized PTFE-H filter (Hyundai MICRO). Prior to coating, the precursor solutions were mildly stirred at 50 ºC for 10 min in ambient condition to remove unwanted gas molecules might be dissolved in the solutions. The precursor solutions with and without K^+ ion were spin-coated on the TiO_2 film at 4000 rpm for 20 s, where 0.35 mL of diethyl ether was dripped after 10 s spinning time. The transparent brownish adduct film was formed right after deposition, which was heated at 140 ºC for 40 min. The 20 μL of spiro-MeOTAD solution, which was prepared by dissolving 72.3 mg spiro-MeOTAD, 28.8 μL of 4-*tert*-butyl pyridine and 17.5 μL of lithium bis(trifluoromethanesulfonyl)imide (LiTFSI) solution (520 mg Li-TSFI in 1 mL acetonitrile (99.8%, Sigma Aldrich)) in 1 mL of chlorobenzene, was spin-coated on the perovskite layer at 3000 rpm for 20 s. Finally, Au electrode was deposited by using a thermal evaporator at an evaporation rate of 0.05 nm/s. For measuring *in-situ* PL images and ionic mobility under illumination, an interdigitated cell was prepared where the perovskite film was deposited on the m-TiO_2/glass substrate and then approximately 70 nm-thick Au strips were deposited by thermal evaporation through a shadow mask at 3×10^{-6} mbar. Distance between Au electrodes was 200 μm or 150 μm and length of Au electrode was 1 cm. To protect the film from oxygen and water molecules, 40 mg/mL poly(methyl methacrylate) (PMMA) solution dissolved in butyl acetate (anhydrous, 99%, Sigma-Aldrich) was spin-coated on the film at a speed of

2000 rpm for 60 s in the glovebox. The probe station was directly used to contact the electrode using tips.

Characterizations of Solar Cells

Current density-voltage (J-V) curves were measured under AM 1.5G one sun (100 mW/cm^2) illumination using a solar simulator (Oriel Sol 3A, class AAA) equipped with 450 W Xenon lamp (Newport 6280NS) and a Kiethley 2400 source meter. The light intensity was adjusted by NREL-calibrated Si solar cell having KG-5 filter. The device was covered with a metal mask with aperture area of 0.125 cm^2.

Photoluminescence Imaging Microscopy

In-situ PL images were measured with a home-built PL microscope [S1-S4]. In detail, on a commercial microscopy (Microscope Axio Imager. A2m, Zeiss) the sample was put in the focal plane of an objective lens (10×/0.25 HD, Zeiss), and a motorized scanning stage (EK 75×50, Märzhäuser Wetzlar GmbH & Co. KG) was used to adjust the position of the samples. An external blue LED illuminator (continuous mode) using a dichroic mirror and filter combination (HC 440 SP, AHF Analysentechnik AG) with the excited wavelength of around 440 nm were used as the illumination source. This allowed for a nearly uniform illumination area on the sample. The excitation light intensity was set to 23.3 mW/cm^2. The PL signal was filtered (HC-BS 484, AHF analysentechnik AG) for the emitted PL signal from the sample. As a result, the wavelength of excitation beam was up to 440nm and the emission signal comes to detector was above 490nm. PL images was recorded by a fast speed CCD camera (Pco. Pixelfly, PCO AG) with the exposure time of 200 ms. A constant voltage was applied between the Au electrodes using an impedance analyzer (PGSTAT 204, Metrohm Autolab).

Impedance Spectroscopy (IS) Measurement

The IS (PGSTAT 204, Metrohm Autolab) was carried, where DC voltage was applied from 0.1 V to 0.5 V at 0.1 V intervals with a 20 mV (RMS) AC voltage perturbation with frequencies ranging from 10 mHz to MHz in the dark. Devices with interdigitated Au/PSK/Au structure were prepared, where channel width between Au electrodes was 200

μm. The fitting results are described in detail in **Fig. S7**, **Table S2** and **Fig. S8** in the supporting information.

X-ray diffraction (XRD) Measurements

The XRD patterns of $(FAPbI_3)_{0.875}(CsPbBr_3)_{0.125}$ perovskite doped with KI or KBr ($[K^+]/[Pb^{2+}]$=0, 0.005, 0.01) and $(FAPbI_3)_{0.875}(CsPbI_3)_{0.125}$ perovskite doped with KI or KBr ($[K^+]/[Pb^{2+}]$=0, 0.005, 0.01) were obtained using a Rigaku Smart Lab SE (40 kV, 40 mA) under graphite-monochromated Cu-Kα radiation at 2 theta interval of 0.01º and the scan rate of 1 º/min. To avoid thermal expansion, the temperature of 290 K was maintained. XRD data were analyzed using EXPO2014 program. To determine space group and crystal structure, we analyzed the XRD data according to the program provided by http://www.ba.ic.cnr.it/softwareic/expo/general-information/. The indexing process was performed by the N-TREOR setting in EXPO2014. Reflections were indexed by cubic unit cell based on Pm-3m space group. The structural parameters of heavy atoms such as Cs, Pb and I were determined by using the direct method in the EXPO2014 software [S5].

Electro Absorption (EA) Spectroscopy

The light source was installed in a monochromator illuminator (Oriel Company). The light going through the monochromator (SPEX 1681B, Horiba Scientific) was illuminated on the device and then the light was reflected back from the electrode onto a photodiode (HUV-4000B, EG&G Judson). A dual channel lock-in amplifier (SR 830 from Stanford Research Systems) was used to bias the device with a DC and an AC voltage and monitored the AC amplitude of the EA signal from the photodiode. In parallel the DC amplitude of the EA signal was recorded with a digital multimeter (HP34401A). For all the electrical experiment, the FTO electrode was connected to the ground, and Au electrode was applied external voltages [S6].

X-ray Photoelectron Spectroscopy (XPS) Depth Profile Measurement

A Gas Cluster Ion Gun (GCIB) is used as sputtered source to obtain a vertical profile of the K+ distribution. XPS measurements were carried with PHI 5000 VersaProbe III system. The X-ray source is an Al Kα excitation source (hν = 1486.6 eV) with a pass energy of 55 eV. The sputtering energy of GCIB is 10kV30nA and each cycle is 2 min.

Conflicts of interest

There are no conflicts to declare

Author Contributions

N.-G.P., J.B. and S.H. conceived this work. S.-G.K., C.L. and A.G. conducted experiments. N.-G.P. and S.-G.K. prepared manuscript. S.-G.K. and J.-M.Y. characterized J-V curves and X-ray diffraction patterns. S.-G.K., C.L. and Z.Y. measured and analyzed PL image and electro absorption spectroscopy (EA). C.L. measured and analyzed ion mobility under illumination. A.G measured impedance spectroscopy (IS) measurements. A.G. and J.B. analyzed and interpreted the results. All authors discussed the results and commented on the manuscript.

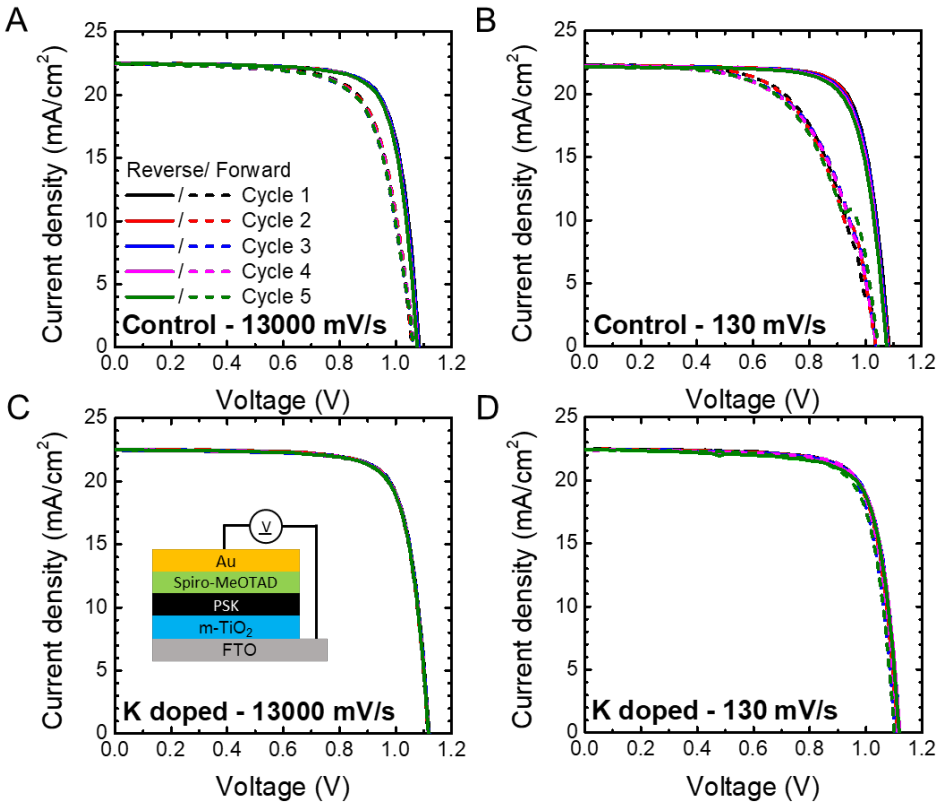

Fig. S1. 5 cycles of J-V curves of $(FAPbI_3)_{0.875}(CsPbBr_3)_{0.125}$ perovskite solar cells without (A, B, C) and with potassium ion doping (D, E, F) ($[K^+]/[Pb^{2+}] = 0.01$) which are measured with different scan rates ((A), (D) - 13000 mV/s and (B), (E) - 130 mV/s, (C), (F) - 13 mV/s) and scan direction under 293 K and AM 1.5G one sun illumination (100 mW/cm^2) conditions. Dashed lines indicate forward scan (from J_{SC} to V_{OC}) while solid lines indicate reverse scan (from V_{OC} to J_{SC}). Aperture mask area was 0.125 cm^2.

Table S1. Photovoltaic properties of 5 cycles of J-V curves with and without K doping $(FAPbI_3)_{0.875}(CsPbBr_3)_{0.125}$ mixed perovskite are measured with different scan rates.

Device ID	J_{sc} (mA/cm^2)	V_{oc} (V)	FF	PCE(%)
Control-Rev-13000mv/s-Cycle1	22.485	1.0824	0.7812	19.01
Control-Rev-13000mv/s-Cycle2	22.495	1.0774	0.7811	18.93
Control-Rev-13000mv/s-Cycle3	22.516	1.0801	0.7808	18.99
Control-Rev-13000mv/s-Cycle4	22.479	1.0761	0.7791	18.85
Control-Rev-13000mv/s-Cycle5	22.496	1.0748	0.7787	18.83
Control-For-13000mv/s-Cycle1	22.555	1.056	0.7311	17.41
Control-For-13000mv/s-Cycle2	22.499	1.0572	0.7284	17.33
Control-For-13000mv/s-Cycle3	22.477	1.0597	0.7219	17.19
Control-For-13000mv/s-Cycle4	22.504	1.062	0.72	17.21
Control-For-13000mv/s-Cycle5	22.482	1.06	0.7207	17.17

Device ID	J_{sc} (mA/cm^2)	V_{oc} (V)	FF	PCE(%)
Control-Rev-130mv/s-Cycle1	22.265	1.0841	0.7763	18.74
Control-Rev-130mv/s-Cycle2	22.232	1.0814	0.7736	18.60
Control-Rev-130mv/s-Cycle3	22.225	1.0788	0.7728	18.53
Control-Rev-130mv/s-Cycle4	22.188	1.0766	0.7693	18.38
Control-Rev-130mv/s-Cycle5	22.155	1.0754	0.7679	18.30
Control-For-130mv/s-Cycle1	22.287	1.0372	0.6261	14.47
Control-For-130mv/s-Cycle2	22.244	1.0387	0.6159	14.23
Control-For-130mv/s-Cycle3	22.214	1.0398	0.6125	14.15
Control-For-130mv/s-Cycle4	22.196	1.0411	0.6082	14.05
Control-For-130mv/s-Cycle5	22.174	1.0456	0.5983	13.87

Device ID	J_{sc} (mA/cm^2)	V_{oc} (V)	FF	PCE(%)
Control-Rev-13mv/s-Cycle1	22.010	1.0817	0.7523	17.91
Control-Rev-13mv/s-Cycle2	21.796	1.0798	0.7458	17.55
Control-Rev-13mv/s-Cycle3	21.560	1.0742	0.7400	17.14
Control-Rev-13mv/s-Cycle4	21.382	1.0733	0.7339	16.84
Control-Rev-13mv/s-Cycle5	21.178	1.0717	0.7296	16.56
Control-For-13mv/s-Cycle1	21.992	1.0823	0.6372	15.17
Control-For-13mv/s-Cycle2	21.813	1.0801	0.6195	14.60
Control-For-13mv/s-Cycle3	21.617	1.0780	0.6028	14.05
Control-For-13mv/s-Cycle4	21.420	1.0785	0.5984	13.82
Control-For-13mv/s-Cycle5	21.214	1.0781	0.5794	13.25

Device ID	J_{sc} (mA/cm^2)	V_{oc} (V)	FF	PCE(%)
Kdoped-Rev-13000mv/s-Cycle1	22.499	1.1175	0.7828	19.68
Kdoped-Rev-13000mv/s-Cycle2	22.498	1.1157	0.7825	19.64
Kdoped-Rev-13000mv/s-Cycle3	22.484	1.116	0.782	19.62
Kdoped-Rev-13000mv/s-Cycle4	22.486	1.1149	0.7814	19.59
Kdoped-Rev-13000mv/s-Cycle5	22.483	1.1149	0.7795	19.54
Kdoped-For-13000mv/s-Cycle1	22.493	1.1135	0.7824	19.6
Kdoped-For-13000mv/s-Cycle2	22.499	1.114	0.7818	19.59
Kdoped-For-13000mv/s-Cycle3	22.48	1.1176	0.7818	19.64
Kdoped-For-13000mv/s-Cycle4	22.483	1.1161	0.7815	19.61
Kdoped-For-13000mv/s-Cycle5	22.486	1.1151	0.7791	19.54

Device ID	J_{sc} (mA/cm^2)	V_{oc} (V)	FF	PCE(%)
Kdoped-Rev-130mv/s-Cycle1	22.457	1.1104	0.7783	19.41
Kdoped-Rev-130mv/s-Cycle2	22.442	1.1118	0.7779	19.41
Kdoped-Rev-130mv/s-Cycle3	22.441	1.1158	0.7766	19.45
Kdoped-Rev-130mv/s-Cycle4	22.433	1.1177	0.7715	19.34
Kdoped-Rev-130mv/s-Cycle5	22.429	1.1158	0.7693	19.25
Kdoped-For-130mv/s-Cycle1	22.46	1.1126	0.7789	19.46
Kdoped-For-130mv/s-Cycle2	22.437	1.1097	0.7786	19.39
Kdoped-For-130mv/s-Cycle3	22.436	1.099	0.7763	19.14
Kdoped-For-130mv/s-Cycle4	22.415	1.0997	0.7724	19.04
Kdoped-For-130mv/s-Cycle5	22.419	1.0986	0.7663	18.87

Device ID	J_{sc} (mA/cm^2)	V_{oc} (V)	FF	PCE(%)
Kdoped-Rev-13mv/s-Cycle1	22.419	1.1105	0.7728	19.24
Kdoped-Rev-13mv/s-Cycle2	22.404	1.1096	0.7681	19.09
Kdoped-Rev-13mv/s-Cycle3	22.394	1.1105	0.7641	19.00
Kdoped-Rev-13mv/s-Cycle4	22.388	1.1109	0.7601	18.90
Kdoped-Rev-13mv/s-Cycle5	22.371	1.1116	0.7584	18.86
Kdoped-For-13mv/s-Cycle1	22.417	1.1074	0.7734	19.20
Kdoped-For-13mv/s-Cycle2	22.407	1.1044	0.7661	18.96
Kdoped-For-13mv/s-Cycle3	22.369	1.1076	0.765	18.95
Kdoped-For-13mv/s-Cycle4	22.318	1.1051	0.7585	18.71
Kdoped-For-13mv/s-Cycle5	22.308	1.103	0.7569	18.62

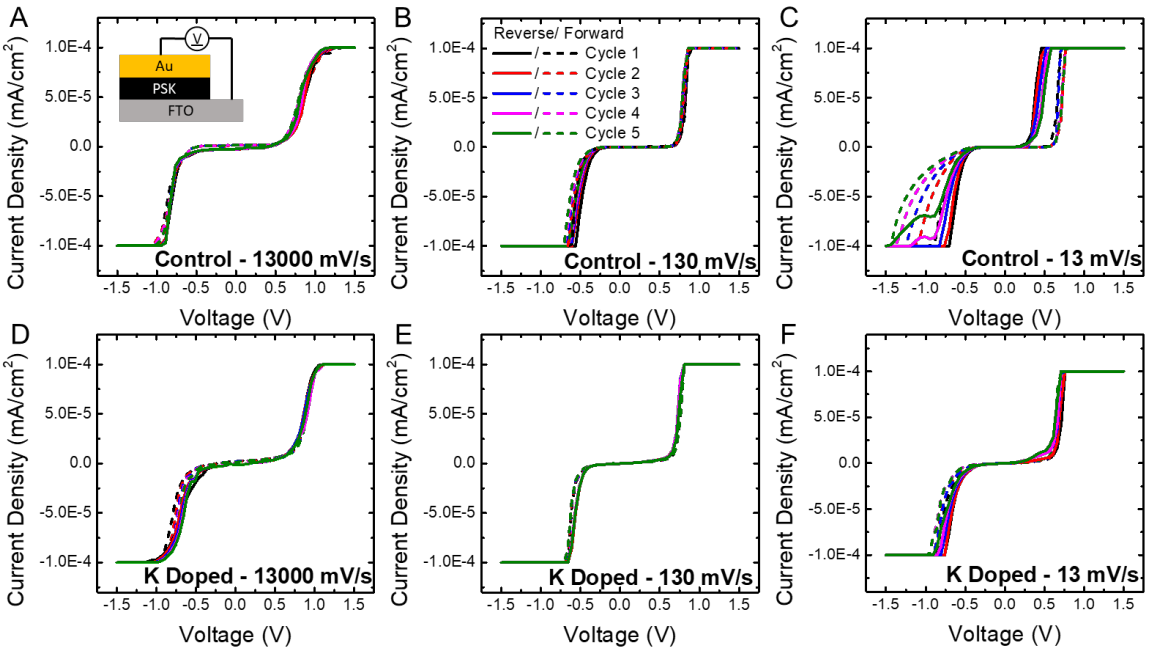

Fig. S2. 5 cycles of I–V curves of FTO/PSK/Au structured devices without (A, B, C) and with potassium ion doping (D, E, F) ($[K^+]/[Pb^{2+}]$ = 0.01) which are measured 5 cycles continuously from 1.5 V to -1.5 V and to 1.5 V without interval time with different scan rates ((A), (C) - 13000 mV/s, (B), (D) - 130 mV/s and (C), (F) - 13 mV/s) and scan direction under 293 K in the dark. The compliance current (CC) was set 10^{-4} A

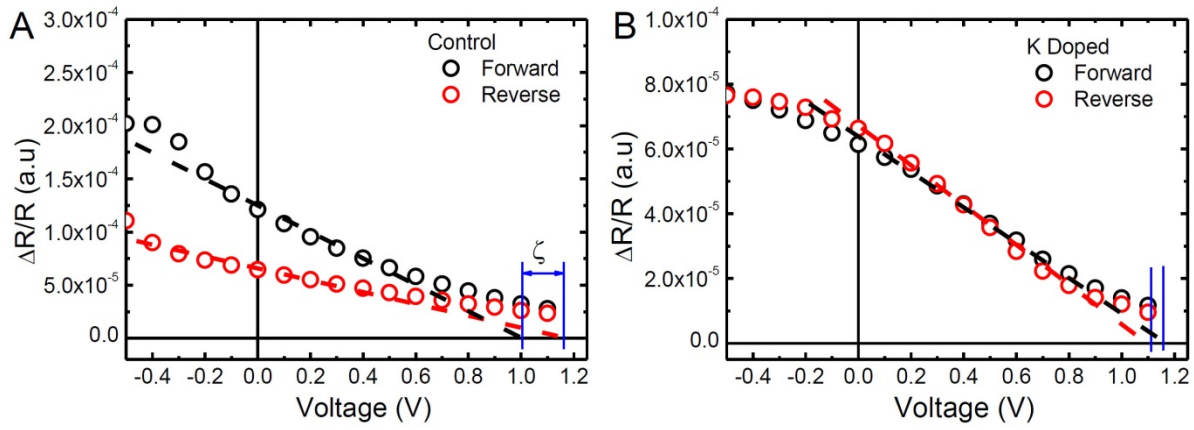

Fig. S3. DC dependent EA signal change (ΔR/R) at photon energy of 1.63 eV for (A) control device and (B) K ion doped device with different scan direction. Built-in-potential difference between forward and reverse is designated as ζ.

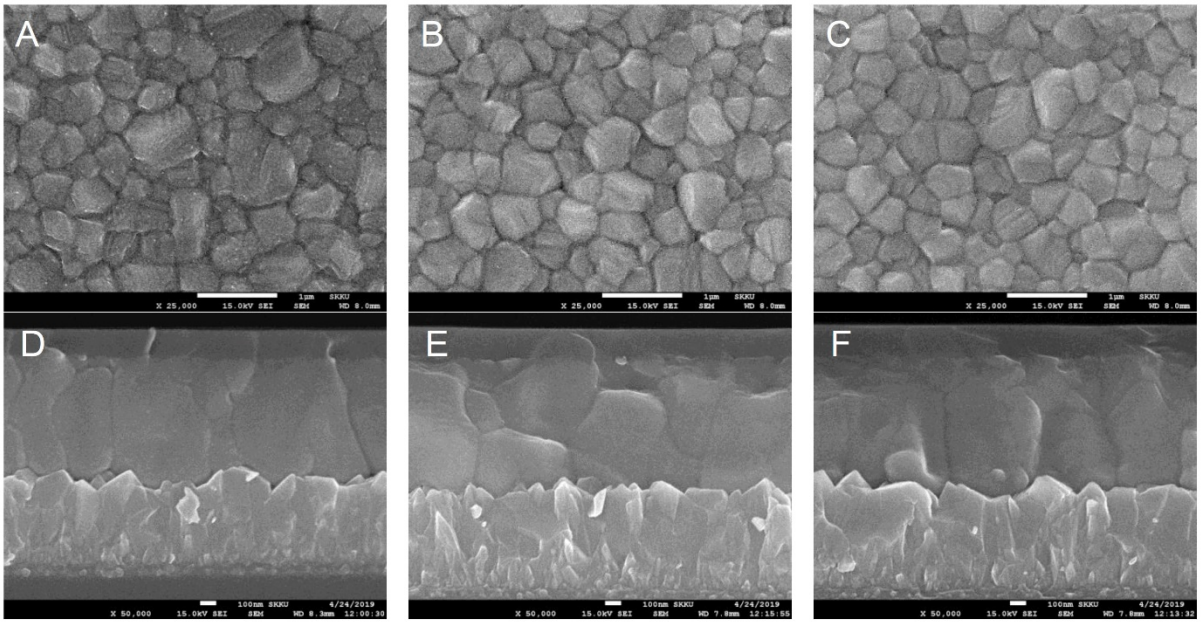

Fig. S4. Plan-view (FTO/TiO_2/PSK) and cross-sectional (FTO/TiO2/PSK/spiro-MeOTAD) SEM images of (A, D) $MAPbI_3$, (B, E) undoped $(FAPbI_3)_{0.875}(CsPbBr_3)_{0.125}$ and (C, F) K^+-doped $(FAPbI_3)_{0.875}(CsPbBr_3)_{0.125}$. Scale bar is 1 μm in (A-C) and 100 nm in (D-F).

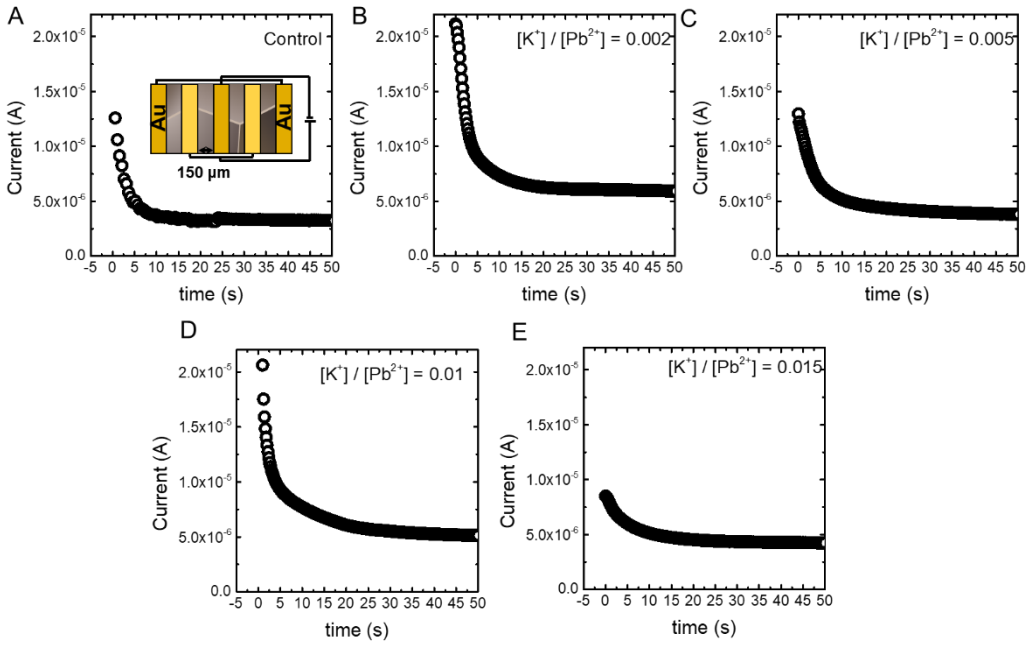

Fig S5. Plots of the current(j) against time (t) with different ratio of K dopant at applied voltage of 4 V. Inset of (A) is schematic representation of lateral device with channel width of 150 µm

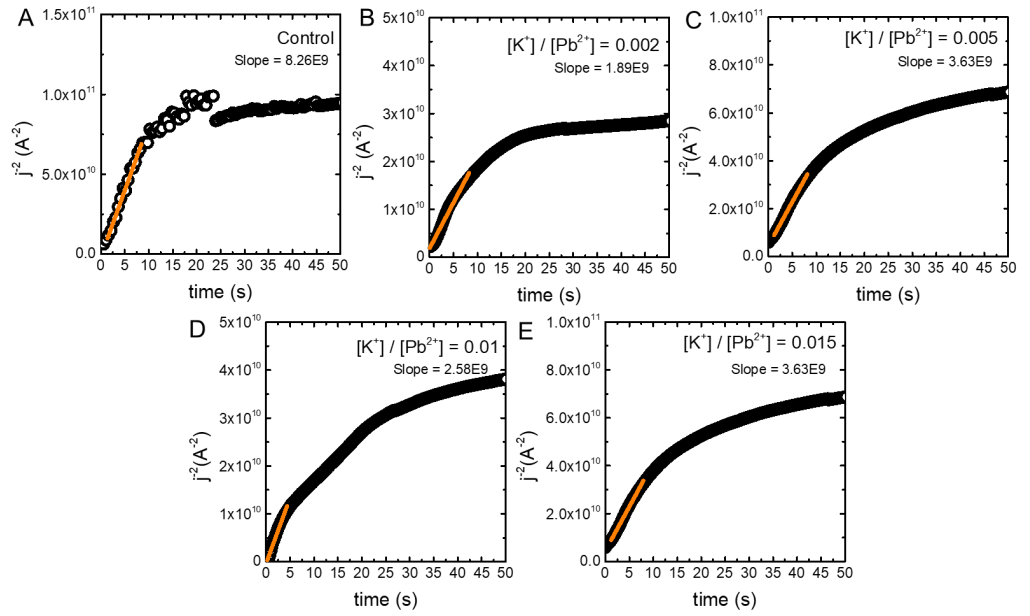

Fig S6. Plots of the current as j^{-2} (A^{-2}) against time (s) with different ratio of K dopant at applied voltage of 4 V.

Impedance spectroscopy fitting

The transmission line model for ionic transport (**Fig. S7**) can be applied successfully to fit the impedance spectroscopy data as can be observed in **Fig. 3**.

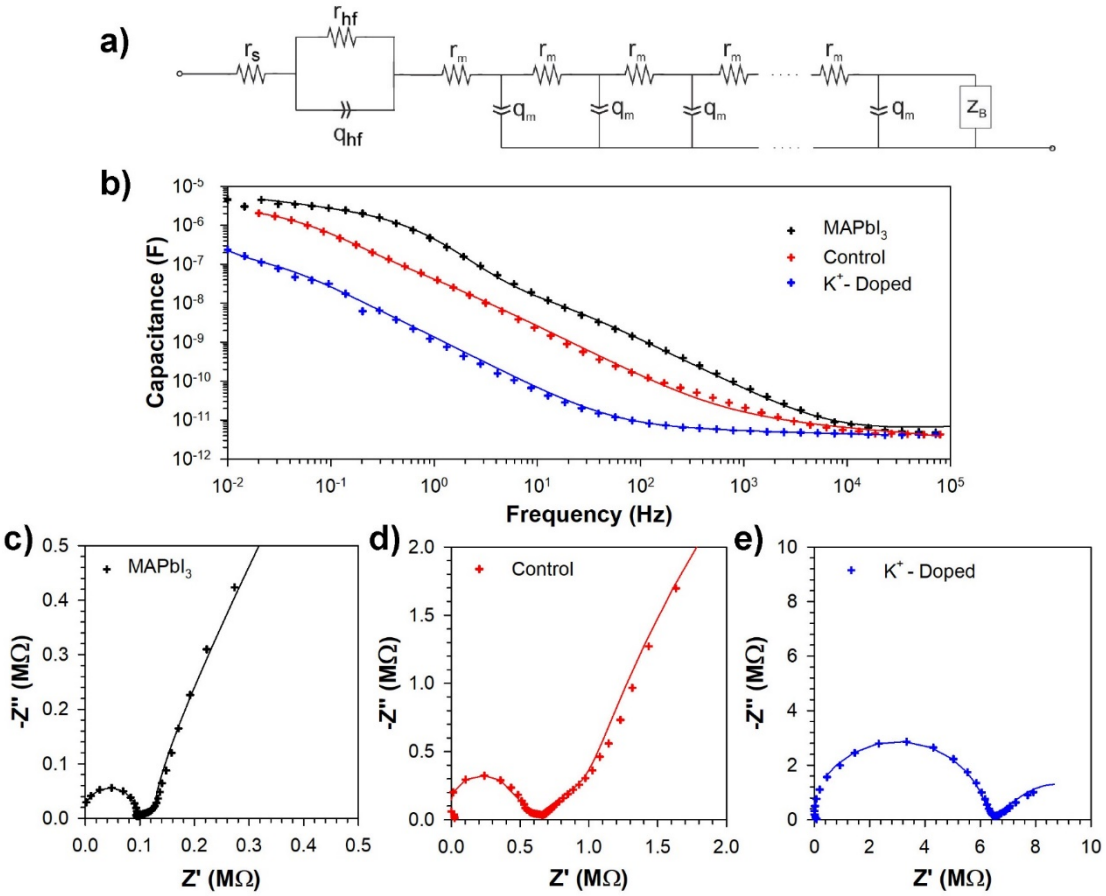

Fig. S7. a) Transmission line model used to fit the experimental data. Comparison of data points measured and fitting results using an equivalent circuit containing a transmission line as show in the inset. Symbols are measured data points and solid line fitting results. b) Capacitance frequency plot. c-e) Complex impedance plots.

The extracted parameters summarized in **Table S2** show errors <10 % except for the sample doped with K^+. In this latter case, the frequency at which accumulation of ions is visible is not observed in the spectrum therefore fittings for the sample doped with K^+ provides large errors for the two capacitors from the transmission line.

Table S2. Extracted parameters from the transmission line equivalent circuit. Exponential factors of the constant phase elements are omitted for simplicity, adopt values from 0.9-1.

Sample	R_{HF}/ Ω	R_m/ Ω	Q_m/ F	Q_{ZB}/ F
MAPI	1.66×10^{5}	5.43×10^{5}	1.00×10^{-6}	2.38×10^{-5}
Control	9.41×10^{5}	8.26×10^{6}	2.39×10^{-8}	1.84×10^{-5}
K+ doped	6.07×10^{6}	6.54×10^{7}	5.31×10^{-5} [(a)]	2.18×10^{-5} [(a)]

[(a)] Fittings for the sample doped with K^+ provides large errors for the two capacitors from the transmission line since the frequency at which accumulation of ions is visible is not observed in the spectrum.

Alternatively, fitting to impedance data to either three or two arcs does not provide adequate fitting as can be observed in **Fig. S8**. Here the exponential factors for constant phase elements have been kept constant at 0.8 since fitting results provided values lower than 0.4 and in this case the system does not behave any longer as a capacitor.

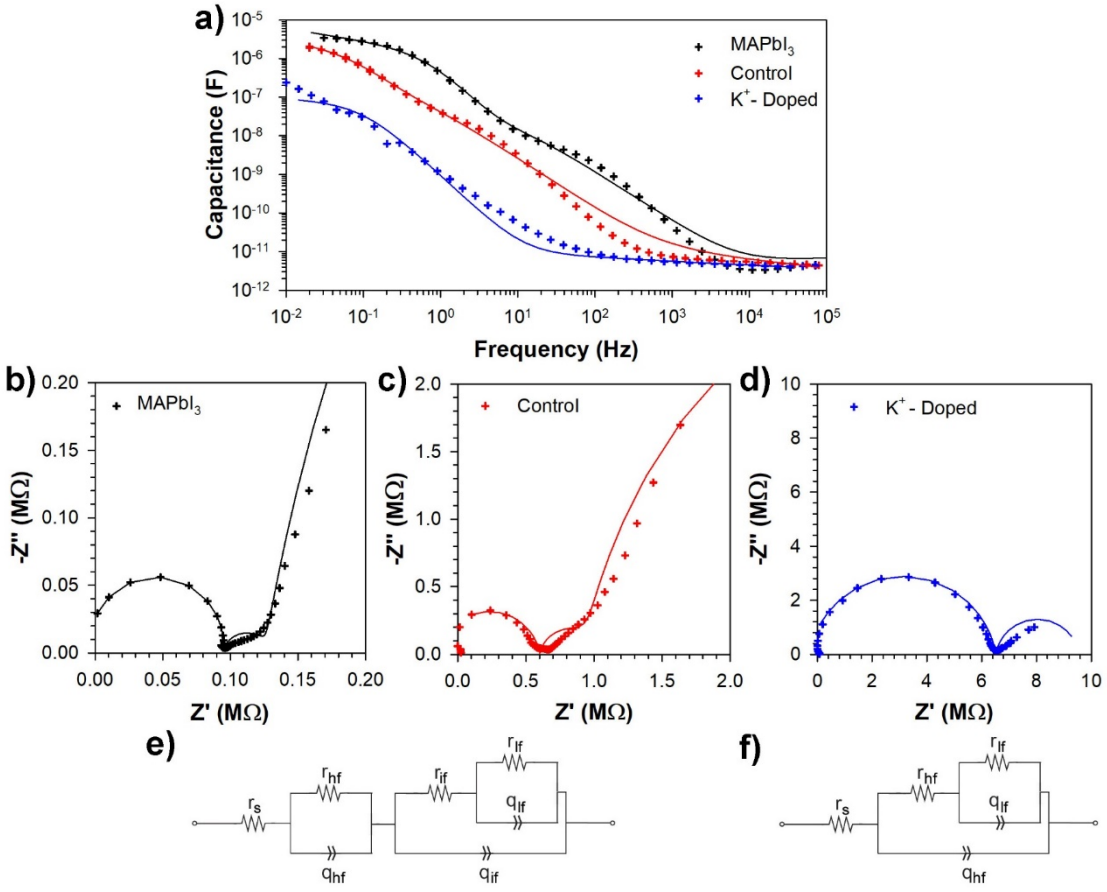

Fig. S8. Comparison of data points measured and fitting results using an equivalent circuit containing a transmission line as show in the inset. Symbols are measured data points and solid line fitting results. a) Capacitance frequency plot. b-d) Complex impedance plots. e) Equivalent circuit used to fit three arcs for $MAPbI_3$ and control sample. e) Equivalent circuit used to fit two arcs for K^+ samples.

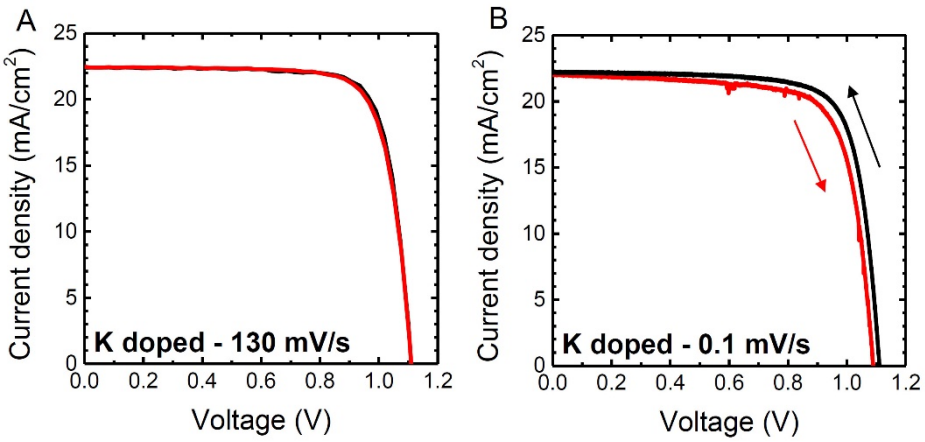

Fig. S9. J-V curves of K+-doped $(FAPbI_3)_{0.875}(CsPbBr_3)_{0.125}$ measured at scan rate of (A) 130 mV/s and (B) 0.1 mV/s. Arrows indicate scan directions.

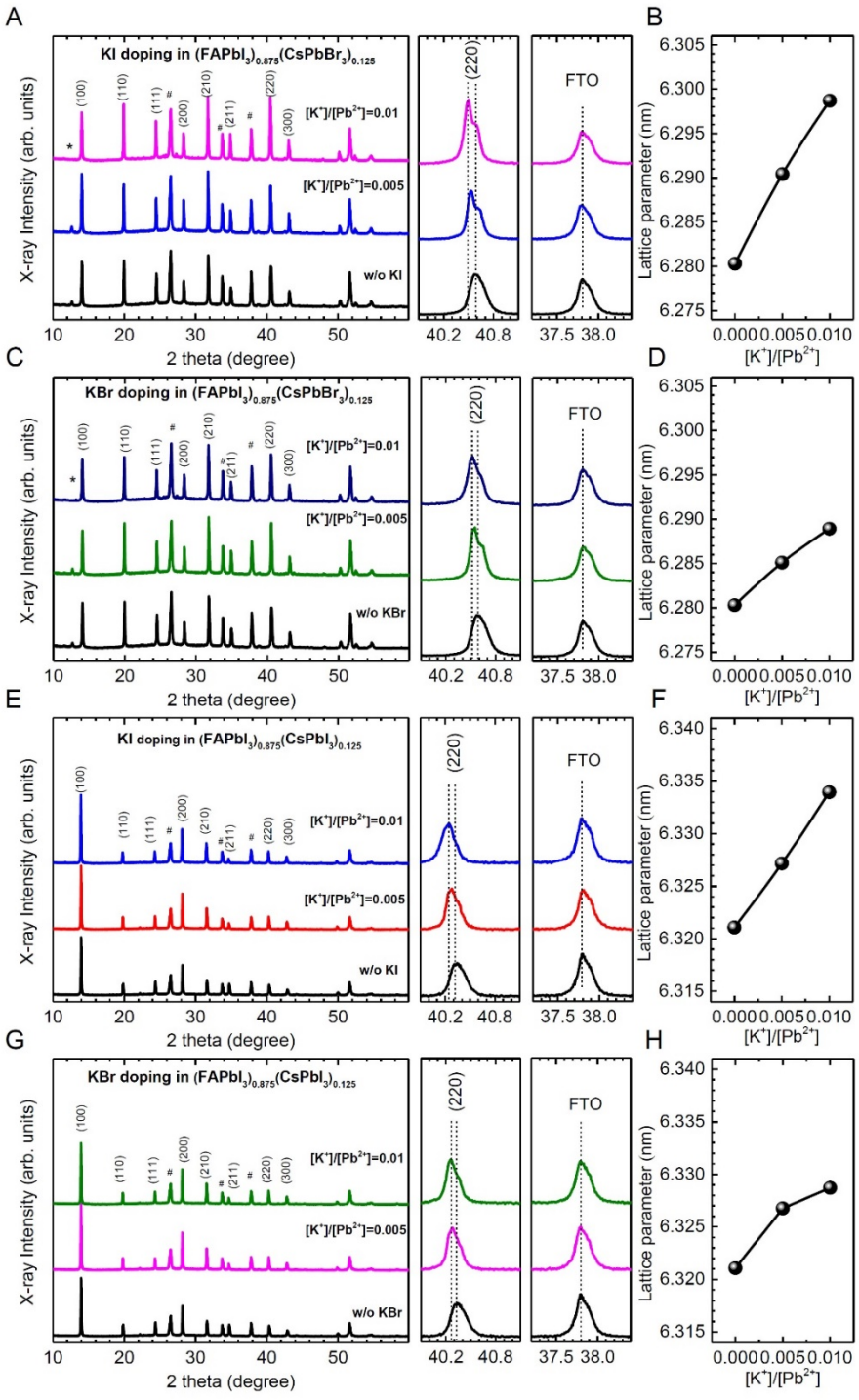

Fig. S10. X-ray diffraction patterns and calculated lattice parameters of $(FAPbI_3)_{0.875}(CsPbBr_3)_{0.125}$ doped with (A, B) KI and (C, D) KBr and $(FAPbI_3)_{0.875}(CsPbI_3)_{0.125}$ doped with (E, F) KI and (G, H) KBr. XRD data were collected under 2 theta interval of 0.01°. It is noted that the peak corresponding to FTO was not changed by doping.

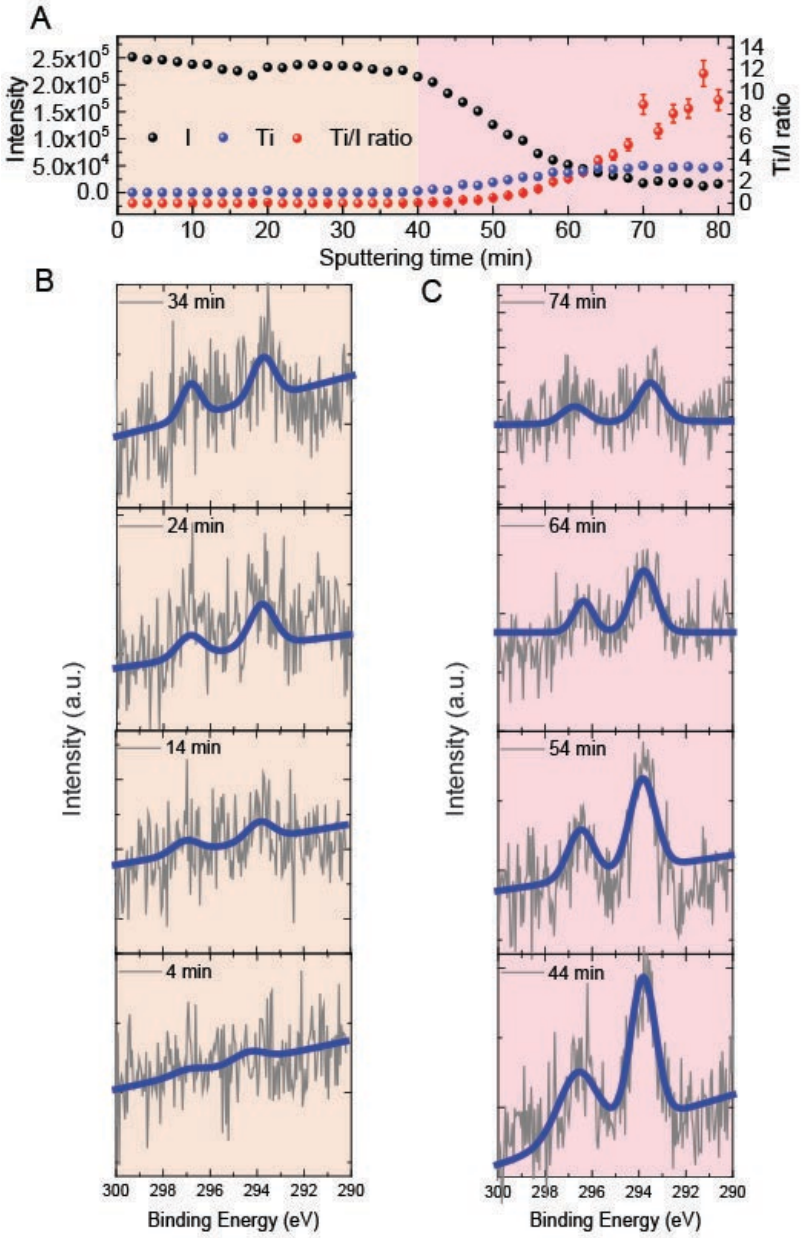

Fig. S11. XPS (Photoelectron spectroscopy) depth profiling using a Gas Cluster Ion Gun (GCIB) in order to obtain a vertical profile of the K^+ distribution. (A) The atomic ratio of Ti/I through the film indicates the thickness of the film as sputtering continues. After sputtering of 40 min, Ti Signal is detected, which means that the mesoporous layer is reached. The K^+ doping level of the perovskite $[K^+]/[Pb^{2+}]$ is 0.01. (B) The XPS spectra of K 2p within the first 40 min sputtering time. It indicates that at the surface, the K amount is small and stays constant throughout the hole film. (C) XPS spectra of K 2p with sputtering time from 40 min to 80 min. The intensity of the K 2p peak reveals more K is detected within the mesoporous TiO_2 than the top perovskite layer.

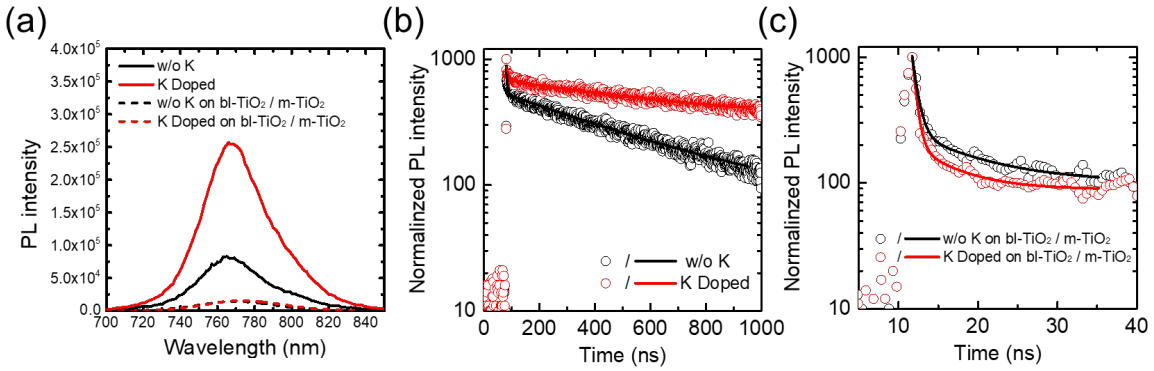

Fig. S12. (a) Steady-state photoluminescence (PL) and (b) time-resolved PL (TRPL) spectra of the $(FAPbI_3)_{0.875}(CsPbBr_3)_{0.125}$ perovskite film without and doped with potassium iodide. (c) TRPL spectra of the $(FAPbI_3)_{0.875}(CsPbBr_3)_{0.125}$ perovskite film without and doped with potassium iodide in contact with bl-TiO_2/m-TiO_2.

Table S3. Fitted results which obtained from the TRPL data in Fig. S12 (b) and (c).

	w/o K	K doped	TiO_2/ w/o K	TiO_2/ K doped
A_1	1069.56 (72.84%)	88.77 (19.3%)	817.79 (84.9%)	745.25 (87.3%)
τ_1 (ns)	2.07	8.81	0.71	0.54
A_2	398.93 (27.16%)	371.74 (80.7%)	145.87 (15.1%)	108.46 (12.7%)
τ_2 (ns)	494.89	705.64	8.71	5.53

References

S1. C. Li, A. Guerrero, Y. Zhong, A. Gräser, C. A. M. Luna, J. Köhler, J. Bisquert, R. Hildner, S. Huettner, Real-Time Observation of Iodide Ion Migration in Methylammonium Lead Halide Perovskites. *Small*. **13**, 1701711 (2017).

S2. A. Issac, R. Hildner, C. Hippius, F. Würthner, J. Köhler, Stepwise Decrease of Fluorescence versus Sequential Photobleaching in a Single Multichromophoric System. *ACS Nano*. **8**, 2, 1708-1717 (2018).

S3. C. Li, Y. Zhong, C. A. M. Luna, T. Unger, K. Deichsel, A. Gräser, J. Köhler, A. Köhler, R. Hildner, Sven Huettner, Emission Enhancement and Intermittency in Polycrystalline Organolead Halide Perovskite Films. *Molecules.* **21**, 1081(2016).

S4. A.T. Haedler, K. Kreger, A. Issac, B, Wittmann, M, Kivala, N. Hammer, J. Köhler, H.-W. Schmidt, R. Hildner, Long-range energy transport in single supramolecular nanofibres at room temperature. *Nature*. **523**, 196–199. (2015).

S5. A. Altomare, C. Cuocci, C. Giacovazzo, A. Moliterni, R. Rizzi, N. Corriero, A. Falcicchio, EXPO2013: a kit of tools for phasing crystal structures from powder data. *J. Appl. Crystallogr*. **46**, 1231–1235 (2013).

S6. C. Li, S. Tscheuschner, F. Paulus, P. E. Hopkinson, J. Kießling, A. Köhler, Y. Vaynzof, S. Huettner, Iodine Migration and its Effect on Hysteresis in Perovskite Solar Cells. *Adv. Mater*. **28**, 2446–2454 (2016).